2007

Secondary Neutron-Production Cross Sections from Heavy-Ion Interactions between 230 and 600 MeV/nucleon

Lawrence H Heilbronn

lheilbro@utk.edu

Recommended Citation

Secondary Neutron-Production Cross Sections from Heavy-Ion Interactions between 230 and 600 MeV/nucleon

L. Heilbronn[(1)§], C. J. Zeitlin[(1)], Y. Iwata[(2)], T. Murakami[(2)], H. Iwase[(3)#], T. Nakamura[(3)], T. Nunomiya[(3)+], H. Sato[(3)*], H. Yashima[(3)¢], R.M. Ronningen[(4)], and K. Ieki[(5)]

(1) MS 74-197, Lawrence Berkeley National Laboratory, Berkeley, CA, 94720
(2) Department of Accelerator Physics and Engineering, National Institute of Radiological Sciences, 4-9-1 Anagawa, Inage, Chiba 263-8555, Japan
(3) Cyclotron and Radioisotope Center, Tohoku University, Aoba, Aramaki, Sendai 980-8578, Japan
(4) National Superconducting Cyclotron Laboratory, Michigan State University, East Lansing, MI 48824-1321
(5) Department of Physics, Rikkyo University, 3-34-1 Nishi Ikebukuro, Toshima, Tokyo 171-8501, Japan
Present address: Gesellschaft für Schwerionenforschung, Darmstadt, Germany
* Present address: Isogo Nuclear Engineering Center, Toshiba Co. 8 Shinsugita-Cho, Isogo-Ku, Yokohama 235-8523, Japan
+ Present address: Fuji Electric Systems Co., Ltd., Radiation Equipment Dept., Tokyo Factory, 1, Fuji-machi, Hino-city, Tokyo 191-8502, Japan
¢ Present address: Reactor Research Institute, Kyoto University,
§ E-mail: LHHeilbronn@LBL.gov

Contact author:
Lawrence Heilbronn
MS 74-197
Lawrence Berkeley National Laboratory
Berkeley, CA 94720
lhheilbronn@lbl.gov
fax: 510-486-6949

Number of pages (double spaced): 64
Number of figures: 30
Number of tables: 7

Abstract - Secondary neutron-production cross-sections have been measured from interactions of 230 MeV/nucleon He, 400 MeV/nucleon N, 400 MeV/nucleon Kr, 400 MeV/nucleon Xe, 500 MeV/nucleon Fe, and 600 MeV/nucleon Ne interacting in a variety of elemental and composite targets. We report the double-differential production cross sections, angular distributions, energy spectra, and total cross sections from all systems. Neutron energies were measured using the time-of-flight technique, and were measured at laboratory angles between 5° and 80°. The spectra exhibit behavior previously reported in other heavy-ion-induced neutron production experiments; namely, a peak at forward angles near the energy corresponding to the beam velocity, with the remaining spectra generated by preequilibrium and equilibrium processes. The double-differential spectra are fitted with a moving-source parameterization. Observations on the dependence of the total cross sections on target and projectile mass are discussed.

I. INTRODUCTION

Advancements in heavy-ion accelerators over the last 30 years have led to the development of several new areas of research, such as hadron radiotherapy for cancer patients, shielding design studies for deep space missions, and the design and construction of high-intensity radioactive beam facilities. For each of these fields, the copious production of secondary neutrons from interactions of the primary heavy-ion beam is a concern. In the case of hadron radiotherapy, as the beam transports through the body to the tumor site, nuclear interactions can produce neutrons, which in turn can lead to dose in healthy tissue outside the treatment area. In the case of shielding for missions in space, the production of neutrons from interactions of galactic cosmic rays (GCR) can make up a significant portion of the total dose received in those missions. For example, theoretical models have shown secondary neutrons to be a major contributor to exposures within lunar habitats and on the Martian surface,[1] and recent studies have shown that neutrons could comprise 30 percent of the dose equivalent on the ISS.[2] In the case of radioactive beam facilities, such as the Department of Energy's planned Rare Isotope Accelerator (RIA) project,[3] the production of secondary neutrons will have an effect on the lifetime of key components in the accelerator, as well as have consequences in the design of the shielding for the facility.

Because of the complexity of the applied research mentioned above, much of the work in those fields involves the use of heavy-ion transport model calculations. Both deterministic and Monte Carlo approaches can be applied to transport model calculations. Both methods have inherent advantages and disadvantages, and as such the application of those methods very much depends on the particular problem being addressed. A

deterministic approach for heavy ion transport in complex media has been developed at the NASA Langley Research Center since the mid 1980s. It has yielded a family of radiation transport codes mainly dedicated to solving engineering problems in radiation-shielding analysis for space missions.[4-6] One of these deterministic codes is the high-charge-and-energy transport code HZETRN, based on the one-dimensional formulation of the Boltzmann transport equation with a straight-ahead approximation[7] and a semi-empirical abrasion-ablation fragmentation model for nuclear fragmentation processes. Using simplifying approximations, the radiation field in and around shielding materials can be calculated by this code with an acceptable accuracy for space research and dosimetry.

Several Monte Carlo computer codes exist, or are in the stage of development, for the simulation of the transport of light and heavy ions in matter. Two codes for the simulation of hadronic cascades (neutrons, protons, pions), HETC[8] and SHIELD,[9] were developed in the early seventies in the US (Oak Ridge) and the former USSR (Dubna), respectively. These two codes have evolved considerably since then. Various spin-offs of HETC have proliferated under the names of HERMES,[10] LAHET[11], MCNPX,[12] NMTC/JAERI,[13] and PHITS.[14,15] HETC itself has recently included heavy-ion interactions.[16,17] Other major Monte Carlo transport codes currently in use that also include heavy-ion interactions (or are in the process of including heavy-ion interactions) are MARS,[18] MCNPX,[12] FLUKA[19-20] and GEANT4.[21]

The validation and verification of the output from transport model calculations depends on a reliable set of experimental nuclear data with which to compare. Until recently, the thin-target (cross sections) and thick-target (yields) neutron-production data

from heavy-ion interactions that was applicable to the general problem of GCR transport was scant. A number of thick-target (stopping-target) neutron yields from high-energy (>100 MeV/nucleon) heavy ion experiments have been published[22-27] which can be used for direct confirmation of transport model calculations of various components of the GCR field. A reliable, calculated database of neutron-production cross sections is needed as input for transport model calculations. As such, a set of experimental cross section data is needed to verify the database of calculated input cross sections. There are some existing heavy-ion neutron-production cross section measurements relevant to GCR transport.[28-34] A compilation of heavy-ion-induced secondary neutron thick-target yields and cross sections is available in a recently published handbook.[35] The handbook contains the data as well as descriptions of the experiments and analyses. The data presented in this work augments other published data to provide a broad base of experimental data suitable for the study of systematics in secondary neutron production.

II. EXPERIMENTAL DETAILS

The measurements took place in between May of 2001 and July of 2003 at the Heavy Ion Medical Accelerator in Chiba (HIMAC) facility of the National Institute of Radiological Sciences (NIRS), Japan. Table I indicates the beam ions, beam energies and targets used in those measurements. The target thicknesses are given in units of g/cm^2. All targets except the Li target were 10-cm by 10-cm square. The Li target was a cylinder with its cylindrical axis aligned along the beam direction. The diameter of the Li target was 5.7 cm.

Figure 1 shows a schematic diagram (not to scale) of the experimental arrangement used for the measurements. The placement of the neutron detectors is

identical in angle and path length to the arrangement described in Refs. 33 and 34, however it is important to note these experiments were conducted on a different beam line at HIMAC than the one used in Refs. 33 and 34. The most important difference in the beam line used for this study is that the beam dump is much closer to the neutron detectors, which required the augmentation of the existing dump on that beam line with additional shielding materials. In Fig. 1, shielding material drawn with diagonal lines is steel (or iron), and the material drawn with the dotted fill is concrete. In order to reduce the number of beam interactions that occur in air between the target location and the beam dump, a thin-walled He-filled tube was placed along the beam axis.

As shown in Fig. 1, neutron detectors were placed between 5° and 80°, at varying flight paths from the target position. Table II contains information regarding the positions of each detector, including the acceptance of the detector given in millisteradians. The flight path lengths indicate the distance from target center to detector center, in cm. Each neutron detector is a cylindrical cell of liquid scintillator (NE-213), 12.7 cm in diameter and 12.7 cm long. The detectors were oriented such that the cylindrical axis was along the line connecting the target center to the detector center. Each detector cell was directly coupled to a 12.7-cm diameter phototube. The intrinsic timing resolution of these detectors, as measured with ^{60}Co source, is on the order of 700-800 ps.

A 5-mm thick, 12.7-cm by 12.7-cm square, solid plastic (NE-102) scintillator (referred to as "veto detector") was placed in front of each neutron detector. The veto detectors were used to tag events in the neutron detectors that came from charged particles produced in the target. A Monte Carlo calculation estimated that approximately

1% of the neutron flux is lost due to interactions in the veto detector. This percentage was considered low enough that neutron losses in the veto detector were ignored.

The iron shadow bars indicated in Fig. 1 were placed between the detector and target at various times during the measurements. These bars were 60-cm long and 15 cm by 15cm square. When placed in front of the neutron detector, they block neutrons coming directly from the target, allowing only background neutrons (such as room-scattered neutrons) to enter the detector. Because neutron energies were determined using the time-of-flight technique, the background neutrons had to be eliminated to ensure that only neutrons travelling along a known flight path were included in the final analysis. Also, the elimination of background neutrons ensures that the direction of the secondary neutron immediately after the interaction was known. A total of two shadow bars were used, and their positions were shifted from detector to detector during the measurements in order that each neutron detector had an adequate determination of its background spectrum. In general, about ¼ of the beam time was used for background determination for each detector.

One major difference in these measurements as compared with the two previously reported measurements[33,34] is that data was also taken with no target in position while beam was on. The no-target runs were taken with shadow bars both in and out. By doing so, a measure of the neutron production from materials near the target (such as the exit window, trigger-plastic detector, and air gap) was obtained. That measurement is needed because when the target is in place and a shadow bar is put into position between the target and detector, the shadow bar also blocks neutrons produced from those nearby

sources. Thus, neutrons produced by nearby sources will be misidentified as neutrons coming from the target, unless a target-out measurement is made.

Beam pulses were delivered on target every 3.3 seconds. Pulse length varied from 0.5 seconds to 1 second, depending on beam ion and energy. Typical pulse intensities varied between 10^4 and 10^5 particles per pulse. The beam spot size was a few millimeters in diameter, and the beam divergence was negligible compared with the spread of the beam due to Coulomb scattering through the target and air. The beam exited the vacuum beam line through a 100-μm-thick aluminum window and passed through either a 0.5-mm-thick or 0.1-mm-thick, 30-cm diameter NE102 scintillator. The scintillator was placed approximately 5 cm downstream from the exit window. That scintillator, referred to as the trigger detector, was used to count the number of beam particles incident upon the target. It was also used to provide a timing signal for a time-of-flight measurement with each event in the neutron detectors. After passing through the trigger detector, the beam then passed through the target position, approximately 19-cm downstream from the exit window. The beam then passed through a 4-meter long, 30-cm diameter He-filled tube and stopped in a beam dump located approximately 7 meters downstream from the target position.

III. ANALYSIS

III.A. Data Reduction, Corrections, and Normalization

The analysis of the data presented in this paper is the same as the analyses reported in Refs. 33 and 34, except in this case there is an additional subtraction of the target-out measurement (see section above). The main points of the analysis will be described here. Detailed descriptions may be found in Refs. 33 and 34.

The data were acquired on an event-by-event basis. Charged particle events in the neutron detectors were separated from other events when the accompanying veto detector registered a pulse height above threshold. Gamma-ray events were separated from neutron events using the pulse-shape-discrimination properties of the NE-213 cells. Neutron energies were determined using a time-of-flight technique where the signal from the neutron detector was used as the timing start, and the signal from the trigger plastic was used as the stop. An absolute time scale was determined by locating the prompt gamma-ray peak in the raw time-of-flight spectra. The overall timing resolution, as measured by the width of the prompt gamma-ray peak, was on the order of 1 nsec for each detector. Where possible, the data were corrected for excessive constant-fraction-discriminator (CFD) walk using an off-line analysis technique.[36] The minimum time-to-digital (TDC) bin-width was set to 1 ns in the offline analysis. Where needed, bin widths were increased to reduce the statistical uncertainty. In general, the statistical uncertainties were kept to 20% or less, although in some cases the statistical uncertainties were higher (up to 50% for some points in the double differential spectra).

The spectra were normalized to the number of incoming beam ions, as measured by the trigger detector. The number of neutron events in a particular energy bin was corrected for the energy-dependent detection efficiency. In general, detection efficiencies ranged between 10 and 40 percent above the pulse height threshold. Pulse-height energy calibration was done for each detector using gamma ray sources and the proton-recoil calibration method.[26]

The spectra were corrected for neutron flux attenuation due to transport through the target and air gap between the target and neutron detector. For the purposes of

transport calculations, it may be preferred to have the data without corrections for neutron flux attenuation. If so desired, the uncorrected data is available in Ref. 35. The amount of attenuation was calculated using a Monte Carlo code that incorporates relevant elastic and non-elastic neutron-scattering cross sections. Some of the neutron-interaction cross-section data bases extend to neutron energies of 1000 MeV; however, most of the data bases used in the code only report cross sections for neutron energies up to 150 MeV. For those cases, cross sections above 150 MeV were assumed to be equal to the value at 150 MeV. For purposes of the calculation, interactions that produce neutrons were assumed to occur at the midpoint of the target. From that point, neutrons were transported through the remaining target and air gap, and neutrons that did not make it to the neutron detector were tallied. Figure 2 shows the percentage of transmitted neutron flux as a function of neutron energy, angle, and target material. Neutron flux attenuation was greatest for the 230 MeV/nucleon He systems, leading to an approximate 15% correction in the total cross section. For other systems with heavier projectiles and thinner targets than the 230 MeV/nucleon He systems, the correction to the total cross sections was as little as 3 to 5 percent. The amount of attenuation is greatest at 80° for all beams and targets.

III.B. Systematic Uncertainties

The systematic uncertainties considered here include estimated and measured effects in: (1) correction for detection efficiency, (2) correction for loss of neutron flux, (3) uncertainty in the solid angle subtended by each detector, (4) uncertainty in the calibration of the charge-to-digital (QDC) data, referred to as "pulse-height calibration" above, and (5) the uncertainty in the number of beam particles counted by the beam

scintillator (trigger detector). A detailed discussion of the how the uncertainties were determined for the first four items may be found in Ref 34. The uncertainty in solid angle may be found in Table II. The uncertainty in the number of beam particles was determined by estimating the number of events that had two beam particles striking the trigger detector close enough in time that they only generated one CFD pulse that was counted. This was determined by looking at the QDC spectrum for the trigger detector, and estimating the number of events that had a total integrated charge that was appreciably greater than the total integrated charge from just one beam particle. The fraction of events that had more than one beam particle depended on beam conditions, but in the worst case it was no greater than four percent of the events. It was conservatively assumed that each beam had an uncertainty of four percent in the number of beam particles.

Table III shows the percent uncertainty for all five items as a function of detector number (re: Table II). The overall systematic uncertainty (column 7 of Table III) was determined by adding the individual uncertainties in quadrature. The systematic uncertainties were applied to the angular distributions and total cross sections.

IV. DOUBLE-DIFFERENTIAL SPECTRA

Figures 3 through 24 show the double differential spectra from all the systems identified in Table I. The error bars represent the statistical uncertainties in the data. The solid lines indicate fits to the data using a moving source parameterization (see discussion below). The spectra shown in Figs. 3 through 24 follow the same general trends seen in similar data.[32-34] The spectra at 5° are dominated by neutrons from the breakup of the

projectile, resulting in a peak that is centered near the beam ion's specific energy (the beam's energy in units of energy-per-nucleon). At 10° and 20°, evidence of neutrons from projectile-like fragments can still be seen, although the peaks are broader and centered at lower energies. The peak or bump at 20° due to projectile fragmentation is most clearly seen for the lighter mass projectiles. At larger angles, the spectra appear to be generated from two distinct sources: (1) Evaporation from the target residues that dominates the spectra below 20 MeV, and (2) decay of the overlap region between the projectile and target that produce neutrons with energies from a few MeV up to hundreds of MeV.

The solid lines in Figs. 3 through 24 show fits to the data using a moving source parameterization. Three sources were assumed in the fitting: (1) breakup of the projectile, (2) breakup of the decay of the overlap region, referred to as pre-equilibrium emission, and (3) decay of the target remnant.

As was done in Ref.33, the projectile-like source was assumed to have the form

$$\frac{d^2\sigma}{p_c^2 dp_c d\Omega_c} = N \exp\left(-\frac{p_c^2}{2\sigma^2}\right), \qquad (1)$$

where p_c is the momentum of the neutron in the rest frame of the source and σ is a width parameter that is related to the internal momentum of nucleons within the source.[37] The double-differential spectra reported here are related to the cross section in Eqn. 1 by

$$\frac{d^2\sigma}{dEd\Omega} = pE_c \frac{d^2\sigma}{p_c^2 dp_c d\Omega_c}, \qquad (2)$$

where E_c is the neutron's kinetic energy in the source's frame, and p is the neutron's momentum in the lab frame. E_c is related to the kinetic energy in the lab frame by

$$E_c = \gamma(E - \beta p \cos\theta),$$ (3)

where β is the source velocity (v/c), γ is the Lorentz factor, and θ is the lab angle.

The other two sources assume an isotropic decay in their rest frame and are given the following Maxwellian form (in the rest frame) as:

$$\frac{d^2\sigma}{p_c^2 dp_c d\Omega_c} = \frac{N}{(2\pi T)^{3/2}} \exp\left(-\frac{p_c^2}{2mT}\right).$$ (4)

Table IV shows the fit parameters for all systems except the 500 MeV/nucleon Fe + CH$_2$ system. The first part of the table shows the parameters from Eqn. 1, and the second half shows the parameters from the two Maxwellian sources described in Eqn. 4. Because there was no data at 5° and 10° for the 500 MeV/nucleon Fe systems, the parameters from Eqn. 1 were difficult to extract for those two systems. In general, the fits are adequate in describing the magnitudes and shape of the spectra between 5° and 80°. Because the moving-source parameterization does not yield unique solutions, these fits are unsuitable for extrapolating to larger angles, or to systems with beam or target masses much different than the ones described here.

V. ANGULAR DISTRIBUTIONS

Figures 25 – 29 show the angular distribution spectra for the indicated systems. The data points, shown with open and closed symbols, were obtained by integrating the experimental double-differential spectra over energy for neutron energies greater than 10 MeV. The error bars include the statistical and systematic uncertainties added together in quadrature. The lines show fits to the data using the following parameterization:

$$d\sigma / d\Omega = a_1 \exp(-a_2\theta) + a_3 \exp(-a_4\theta), \tag{5}$$

where θ is in radians, and a_1, a_2, a_3, and a_4 are the fit parameters. Table V shows the fitted parameters from all systems. The first two terms in Eqn. 5 represent the breakup of the projectile, and the last two terms represent the contribution from the decay of the overlap region and the target remnant. Because no data were taken at 5° and 10° for the 500 MeV/nucleon Fe systems, no fits were made to their angular distributions. The projectile decay parameters for the 400 MeV/nucleon Kr + Pb system and the 400 MeV/nucleon N + C system are anomalous due to fitting the relatively low yield at 10° (see Figs. 25 and 26). All of the systems exhibit a strong focussing of the spectra in the forward direction. Because a neutron energy threshold of 10 MeV was used, a sizable fraction of the yield from the decay of the target remnant is missing, which in effect enhances the forward-focussing of the angular distributions.

VI. TOTAL CROSS SECTIONS

The angular distribution data shown in figs. 25 – 29 were integrated over angle to yield the total cross sections. The angular cross sections at 5° were integrated over the range of 0° to 7.5°, the 10° yields were integrated from 7.5° to 15°, the 20° yields were integrated from 15° to 25°, the 30° yields were integrated from 25° to 35°, the 40° yields

were integrated from 35° to 50°, the 60° yields were integrated from 50° to 70°, and the

80° yields were integrated from 70° to 90°. Table VI shows those results for neutron

energy thresholds of 5 MeV (column three) and 10 MeV (columns 4 – 6), and for yields

with (columns 3, 4, and 6) and without (column 5) corrections for neutron attenuation.

The total cross sections from 0° to 180° were deduced by adding the data-integrated cross

sections from 0° to 90° together with the calculated total cross sections from 90° to 180°.

The total cross sections from 90° to 180° were calculated by integrating Eqn. 5 from 90°

to 180°, using the parameters listed in Table V. Comparing columns 4 and 5 in Table VI,

it is seen that approximately 3 to 8 percent of the total cross section is estimated to be lost

due to neutron flux attenuation, at least for the thinner targets used. For the thicker

targets used with the 230 MeV/nucleon He beams, about 15% of the flux is estimated to

be lost.

Using the total cross sections from 0° to 180° in this work together with the total

cross sections reported in Ref. [Iwata01], it is found that the total cross sections can be

estimated using a simple parameterization that is based on the geometric cross section

and the number of projectile and target neutrons from each system. The parameterization

has the form:

$$\sigma_{neut}(tot) = C \times \left(A_{proj}^{1/3} + A_{targ}^{1/3} \right)^2 \times \left[\left(f_p \times N_p \right) + \left(f_t \times N_t \right) \right], \tag{6}$$

where $\sigma_{neut}(tot)$ is the total secondary-neutron-production cross section from 0° to 180°, C

is a normalization constant, A_{proj} and A_{targ} are the atomic numbers of the projectile and

target, N_p and N_t and the neutron numbers of the projectile and target, and f_p and f_t are the

fraction of projectile and target neutrons contributing to the yield. A global fit to all of

the data using a single set of parameters (C, f_p and f_t) was somewhat successful, yielding a χ^2 of 1.89 per degree of freedom. However, it was found that better results were obtained when the data was split into three categories: (1) light-mass projectile systems (He, C, and N beams), (2) intermediate-mass systems (Ne, Si, and Ar beams), and (3) heavy-mass systems (Kr and Xe beams). Table VII contains the fit parameters from all three categories, along with the fit parameters from the global fit. The last column shows the chi-square per degree of freedom for the corresponding fits; the fits in the individual categories each yield a χ^2 of less than 1 per degree of freedom.

Figure 30 shows the total cross sections from column 6 in Table VI and the data from Table IV in Ref. 33 extended to 180 degrees, along with the fits to the data using Eqn. 6 and the parameters from Table VII. The data for C, N, and O projectiles are shown with the open circles, and the fit to that set of data only (row 2 in Table VI) is shown with the dot-dashed line. The data for Ne, Si, and Ar projectiles are shown with the open triangles, and the fit to that set of data only (row 3 in Table VII) is shown with the dotted line. The data for heavy projectiles (Kr and Xe) are shown with the filled diamond-shaped symbols, and the fit to that data set only (row 4 in Table VII) is shown with the dashed line. The global fit to all the data (row 5 in Table VII) is shown with the solid line.

The trend of the parameters in Table VII as a function of projectile mass (rows 2-4) suggest that as the projectile mass increases, the percentage of target neutrons contributing to the yield also increases. This is consistent with the picture that, averaging over impact parameter, the larger the projectile, the larger the overlap region between target and projectile, and hence a larger fraction of target neutrons participating in the

interaction. The parameters also suggest that as the projectile mass increases, the fraction of projectile neutrons contributing to the neutron yield decreases. This is also consistent with the interaction dynamics described above. Observation of the data in Fig. 30 suggests that the light-mass projectile data (in particular, the C + Pb systems) forces the global fit to underestimate the data from heavier mass projectiles.

VII. Conclusions

Neutron production cross sections, angular distributions and total cross sections were measured in a variety of heavy-ion interactions. Projectile masses ranged from He to Xe, and beam energies ranged between 230 and 600 MeV/nucleon. Targets varied in mass between Li and Pb, and cross sections from a polyethylene target were measured as well. Neutrons were measured between 5 and 80 degrees, and the reported neutron energy thresholds varied between 3 and 10 MeV, depending on angle and system. A moving-source parameterization of the double-differential cross sections was performed, along with a parameterization of the angular distributions. A simple parameterization utilizing just the geometric cross section and neutron number of the target and projectile was performed on the total cross sections above 10 MeV. The systematics inferred from the parameterizations are consistent with the picture of neutron production in heavy-ions collisions: projectile breakup contributing to forward-focussed high energy yield, target evaporation contributing to the low-energy (10-20 MeV and below) yield, and decay of the overlap region contributing to a wide range of neutron energies at a wide range of angles. These data, along with other referenced data, will provide a comprehensive data base of neutron production from medium-energy heavy-ion interactions that will be useful to several transport models that are either working on the inclusion of heavy-ion

interactions, or have just recently made public versions of the codes that do include

heavy-ion interactions.

ACKNOWLEDGEMENTS

REFERENCES

1. L.C. SIMONSEN and J.E. NEALY, "Radiation Protection for Human Missions to the Moon and Mars," Technical Paper 3079, National Aeronautics and Space Administration (1991).

2. E.V. BENTON and G.D. BADHWAR (eds), "Prediction and Measurements of Secondary Neutrons in Space," *Radiat. Meas.* **33** (2001).

3. *"ISOL Task Force Report to NSAC"*, H. GRUNDER (chair), November 22, 1999 (unpublished).

4. J. W. WILSON, L. W. TOWNSEND, H. B. BIDASARIA, W. SCHIMMERLING, M. WONG and J. HOWARD, "Neon-20 depth-dose relations in water", *Health Physics* **46** No 5 (May) 1101-1111 (1984).

5. J. W. WILSON, M. REGINATO, F. HAJNAL and S. Y. CHUN, "Calculation of Dose, Dose Equivalent, and Relative Biological Effectiveness for high Charge and Energy Ions Beams", *Health Physics* **68** 532-538 (1995).

6. J. W. WILSON, R. K. TRIPATHI, G. D. QUALLS, F. A. CUCINOTTA, R. E. PRAEL, J. W. NORBURY, J. H. HEINBOCKEL, J. TWEED and G. De ANGELIS, "Advances in Space Radiation Shielding Codes", *Journal of Radiation Research* **43**:Suppl. S87-S91 (2002).

7. J. W. WILSON, F. F. BADAVI, F. A. CUCINOTTA, J. L. SHINN, G. D. BADHWAR, R. SILBERGER, C. H. TSAO, L. W. TOWNSEND and R. K. TRIPATHI, "HZETRN: Description of a Free-Space Ion and Nucleon transport and Shielding Computer Program", NASA Technical Paper 3495 (1995).

8. T. W. ARMSTRONG and K. G. CHANDLER, "HETC - A High Energy Transport Code", *Nucl.Sci.Eng.* **49** 110-111 (1972).

9. N. M. SOBOLEVSKY, "A code for the simulation of nucleon-meson cascades in matter by the Monte Carlo method", *Report JINR* B1-2-5458 Dubna 1-143 (in Russian) (1970).

10. P. CLOTH, D. FILGES, R. D. NEEF, G. STERZENBACH, Ch. REUL, T. W. ARMSTRONG, B. L. COLBORN, B. ANDERS and H. BRÜCKMANN, "HERMES: A Monte Carlo System for Beam Materials Interaction Studies", *KFA-Report* Jül-2203 (1988).

11. R. E. PRAEL and H. LICHTENSTEIN, "User Guide to LCS: The LAHET Code System", Los Alamos National Laboratory LA-UR-89-3014 (1989).

12. G. HUGHES, K. J. ADAMS, M. B. CHADWICK, J. C. COMLY, S. C. FRANKLE, J. S. HENDRICKS, R. C. LITTLE, R. E. PRAEL, L. S. WATERS, P. G. YOUNG Jr, "MCNPX^{TM} – The LAHET^{TM}/MCNP^{TM} Code Merger", *Proc of Third Workshop on Simulating Accelerator Radiation Environments (SARE 3)* KEK, Tsukuba, Japan, May 7-9 KEK Proceedings 97-5, H/R/D, Ed. H.Hirayama, 44-51 (1997).

13. H. TAKADA, N. YOSHIZAWA, K. KOSAKA, K. ISHIBASHI, "An upgraded version of the nucleon-meson transport code *NMTC-JAERI97"*, JAERI-Data/Code 98-005 (1998).

14. H. IWASE, K. NIITA, and T. NAKAMURA, "Development of General-Purpose Particle and Heavy Ion Transport Monte Carlo", Code *Journal of Nuclear Science and Technology* **39** No. 11 1142-1151 (2002).

15. K. NIITA, T. SATO, H. IWASE, H. NOSE, H. NAKASHIMA, L. SIHVER, "Particle and Heavy Ion Transport Code System; PHITS", *Proc. 2003 Symposium on Nuclear Data*, Nov. 2003, JAERI, Takai, Japan, JAERI-Conf2004-005, pp. 33 (2004).

16. T. M. MILLER and L. W. TOWNSEND, "Comprehensive Cross Section Database Development for Generalized Three Dimensional Radiation Transport Codes", *Nucl. Sci. and Eng.*, Vol. 149, No. 1, January 2005, pp. 65-73.

17. L. W. TOWNSEND, T. M. MILLER and T. A. GABRIEL, "HETC Radiation Transport Code Development for Cosmic Ray Shielding Applications in Space", *Radiation Protection Dosimetry* (2005, in press).

18. N. V. MOKHOV, "The MARS Code System User's Guide", *Fermilab-FN-628* (1995).

19. A. FASSÒ, A. FERRARI, J. RANFT, P. R. SALA, "New Developments in FLUKA Modeling Hadronic and EM Interactions", *Proc. of 3rd Workshop on Simulating Accelerator Radiation Environments (SARE 3)* KEK, Tsukuba, Japan, May 7-9, KEK Proceedings 97-5, H/R/D, Ed. H.Hirayama (1997).

20. A. FERRARI and P. R. SALA, "Intermediate and High Energy Models in FLUKA: Improvements, Benchmarks and Applications", I*nternational Conference on Nuclear Data for Science and technology*, Miramare-Trieste, Italy, May 19-24, ed. By G. Reffo, A. Ventura and C. Grandi, 247-253 (1997).

21. S. AGOSTINELLI et al., GEANT4 Collaboration, "GEANT4 – a simulation tookit", *Nucl. Instrum. Methods A* **506**, 250-303 (2003).

22. R.A. CECIL, B.D. ANDERSON, A.R. BALDWIN, R. MADEY, A. GALONSKY, P. MILLER, L. YOUNG, and F.M. WATERMAN, "Neutron Angular and Energy Distributions from 710-MeV Alphas Stopping in Water, Carbon, Steel, and Lead, and 640-MeV Alphas Stopping in Lead," *Phys. Rev. C* **21**, 2471 (1980).

23. T. KUROSAWA, N. NAKAO, T. NAKAMURA, Y. UWAMINO, T. SHIBATA, N. NAKANISHI, A. FUKUMURA, and K. MURAKAMI, "Measurements of secondary neutrons produced from thick targets bombarded by high energy helium and carbon ions," *Nucl. Sci. and Eng.* **132**, 30-57 (1999).

24. T. KUROSAWA, N. NAKAO, T. NAKAMURA, Y. UWAMINO, T. SHIBATA, A. FUKUMURA, and K. MURAKAMI, "Measurements of Secondary Neutrons Produced from Thick Targets Bombarded by High Energy Neon Ions," *Journ. of Nucl. Sci. and Tech.* 36, 41-53 (1999).

25. T. KUROSAWA, N. NAKAO, T. NAKAMURA, H. IWASE, H. SATO, Y. UWAMINO, and A. FUKUMURA, "Neutron yields from thick C, Al, Cu, and Pb targets bombarded by 400 MeV/nucleon Ar, Fe, Xe and 800 MeV/nucleon Si ions," *Phys. Rev. C* **62**, (2000).

26. L. HEILBRONN, R.S. CARY, M. CRONQVIST, F. DEAK, K. FRANKEL, A. Galonsky, K. HOLABIRD, A. HORVATH, A. KISS, J. KRUSE, R.M. RONNINGEN, H. SCHELIN, Z. SERES, C.E. Stronach, J. WANG, P. ZECHER, and C. ZEITLIN, "Neutron Yields form 155 MeV/Nucleon Carbon and Helium Stopping in Aluminum," *Nucl. Sci. and Eng.* **132** (1999).

27. B.I. BRITVICH, A.A. CHUMAKOV, R.M. RONNINGEN, R.A. BLUE, and L.H. HEILBRONN, "Measurements of thick target neutron yields and shielding studies using beams of ^{4}He, ^{12}C, and ^{16}O at 155 MeV/nucleon from the K1200 cyclotron at the National Superconducting Cyclotron Laboratory," *Rev. Sci. Instrum*. **70**, 2314-2324 (1999).

28. W. SCHIMMERLING, J.W. KAST, D. ORTENDAHL, R. MADEY, R.A. CECIL, B.D. ANDERSON and A.R. BALDWIN, "Measurement of the Inclusive Neutron Production by Relativistic Neon Ions on Uranium," *Phys. Rev. Lett*. **43**, 1985-1987 (1979).

29. R.A. CECIL, B.D. ANDERSON, A.R. BALDWIN, R. MADEY, W. SCHIMMERLING, J.W. KAST, and D. ORTENDAHL, "Inclusive neutron production by 337 MeV/nucleon neon ions on carbon, aluminum, copper, and uranium," *Phys. Rev. C* **24**, 2013-2029 (1981).

30. R. MADEY, B.D. ANDERSON, R.A. CECIL, P.C. TANDY, and W. SCHIMMERLING, "Total inclusive neutron cross sections and multiplicities in nucleus-nucleus collisions at intermediate energies," *Phys. Rev. C* **28**, 706-709 (1983).

31. A.R. BALDWIN, R. MADEY, W.M. ZHANG, B.D. ANDERSON, D. KEANE, J. VARGA and J.W. WATSON, "Inclusive neutron cross sections from Ne-Pb collisions at 790 MeV/nucleon", *Phys. Rev. C* **46**, 258-264 (1992).

32. H. SATO, T. KUROSAWA, H. IWASE, T. NAKAMURA, Y. UWAMINO and N. NAKAO, "Measurements of double differential neutron production cross sections by 135 MeV/nucleon He, C, Ne and 95 MeV/nucleon Ar ions," *Phys. Rev. C* **64**, (2001).

33. Y. IWATA, T. MURAKAMI, H. SATO, H. IWASE, T. NAKAMURA, T. KUROSAWA, L. HEILBRONN, R.M. RONNINGEN, K. IEKI, Y. TOZAWA, and K. NIITA, "Double-differential cross sections for the neutron production from heavy-ion reactions at energies E/A = 290-600 MeV," *Phys. Rev. C* **64**, 054609 (2001).

34. L. HEILBRONN, Y. IWATA, H. IWASE, T. MURAKAMI, H. SATO, T. NAKAMURA, R.M. RONNINGEN, K. IEKI, I. GUDOWSKA, and N. SOBOLEVSKY, "Secondary neutron production cross sections from heavy ion interactions in composite targets", *Phys. Rev C* **73**, 024603 (2006).

35. T. NAKAMURA and L. HEILBRONN, "Handbook on Secondary Particle Production and Transport by High Energy Heavy Ions", World Scientific Publishing, 5 Toh Tuck Link, Singapore 596224 (2006).

36. L. HEILBRONN, Y. IWATA, and H. IWASE, "Off-line correction for excessive constant-fraction-discriminator walk in neutron time-of-flight experiments," *Nucl. Instrum. Methods A* 522, 495-503 (2004).

37. R. SERBER, "The Production of High Energy Neutrons by Stripping", *Phys. Rev*. **72**, 1008 (1947).

FIGURE CAPTIONS

Fig. 1. A schematic view of the experimental arrangement used for the measurements (not to scale).

Fig. 2. The fraction of neutron flux transmitted from the target to the neutron detector as a function of neutron energy. Plots are shown for the four cases indicated in the legend.

Fig. 3. Double-differential spectra from 230 MeV/nucleon He interacting in an Al target. The spectra at each laboratory angle are offset by the indicated factors of 10. The lines come from a moving-source fit described in the text.

Fig. 4. Double-differential spectra from 230 MeV/nucleon He interacting in a Cu target. The spectra at each laboratory angle are offset by the indicated factors of 10. The lines come from a moving-source fit described in the text.

Fig. 5. Double-differential spectra from 400 MeV/nucleon N interacting in a C target. The spectra at each laboratory angle are offset by the indicated factors of 10. The lines come from a moving-source fit described in the text.

Fig. 6. Double-differential spectra from 400 MeV/nucleon N interacting in a Cu target. The spectra at each laboratory angle are offset by the indicated factors of 10. The lines come from a moving-source fit described in the text.

Fig. 7. Double-differential spectra from 400 MeV/nucleon Kr interacting in a Li target. The spectra at each laboratory angle are offset by the indicated factors of 10. The lines come from a moving-source fit described in the text.

Fig. 8. Double-differential spectra from 400 MeV/nucleon Kr interacting in a C target. The spectra at each laboratory angle are offset by the indicated factors of 10. The lines come from a moving-source fit described in the text.

Fig. 9. Double-differential spectra from 400 MeV/nucleon Kr interacting in a CH_2 target. The spectra at each laboratory angle are offset by the indicated factors of 10. The lines come from a moving-source fit described in the text.

Fig. 10. Double-differential spectra from 400 MeV/nucleon Kr interacting in an Al target. The spectra at each laboratory angle are offset by the indicated factors of 10. The lines come from a moving-source fit described in the text.

Fig. 11. Double-differential spectra from 400 MeV/nucleon Kr interacting in a Cu target. The spectra at each laboratory angle are offset by the indicated factors of 10. The lines come from a moving-source fit described in the text.

Fig. 12. Double-differential spectra from 400 MeV/nucleon Kr interacting in a Pb target. The spectra at each laboratory angle are offset by the indicated factors of 10. The lines come from a moving-source fit described in the text.

Fig. 13. Double-differential spectra from 400 MeV/nucleon Xe interacting in a Li target. The spectra at each laboratory angle are offset by the indicated factors of 10. The lines come from a moving-source fit described in the text.

Fig. 14. Double-differential spectra from 400 MeV/nucleon Xe interacting in a C target. The spectra at each laboratory angle are offset by the indicated factors of 10. The lines come from a moving-source fit described in the text.

Fig. 15. Double-differential spectra from 400 MeV/nucleon Xe interacting in a CH$_2$ target. The spectra at each laboratory angle are offset by the indicated factors of 10. The lines come from a moving-source fit described in the text.

Fig. 16. Double-differential spectra from 400 MeV/nucleon Xe interacting in an Al target. The spectra at each laboratory angle are offset by the indicated factors of 10. The lines come from a moving-source fit described in the text.

Fig. 17. Double-differential spectra from 400 MeV/nucleon Xe interacting in a Cu target. The spectra at each laboratory angle are offset by the indicated factors of 10. The lines come from a moving-source fit described in the text.

Fig. 18. Double-differential spectra from 400 MeV/nucleon Xe interacting in a Pb target. The spectra at each laboratory angle are offset by the indicated factors of 10. The lines come from a moving-source fit described in the text.

Fig. 19. Double-differential spectra from 500 MeV/nucleon Fe interacting in a Li target. The spectra at each laboratory angle are offset by the indicated factors of 10. The lines come from a moving-source fit described in the text.

Fig. 20. Double-differential spectra from 500 MeV/nucleon Fe interacting in a CH$_2$ target. The spectra at each laboratory angle are offset by the indicated factors of 10.

Fig. 21. Double-differential spectra from 500 MeV/nucleon Fe interacting in an Al target. The spectra at each laboratory angle are offset by the indicated factors of 10. The lines come from a moving-source fit described in the text.

Fig. 22. Double-differential spectra from 600 MeV/nucleon Si interacting in a C target. The spectra at each laboratory angle are offset by the indicated factors of 10. The lines come from a moving-source fit described in the text.

Fig. 23. Double-differential spectra from 600 MeV/nucleon Si interacting in a Cu target. The spectra at each laboratory angle are offset by the indicated factors of 10. The lines come from a moving-source fit described in the text.

Fig. 24. Double-differential spectra from 600 MeV/nucleon Si interacting in a Pb target. The spectra at each laboratory angle are offset by the indicated factors of 10. The lines come from a moving-source fit described in the text.

Fig. 25. Angular distribution from the 230 MeV/nucleon He systems for $E_n > 10$ MeV. The lines show a fit to the data using Eqn. 5.

Fig. 26. Angular distribution from the 400 MeV/nucleon N systems for $E_n > 10$ MeV. The lines show a fit to the data using Eqn. 5.
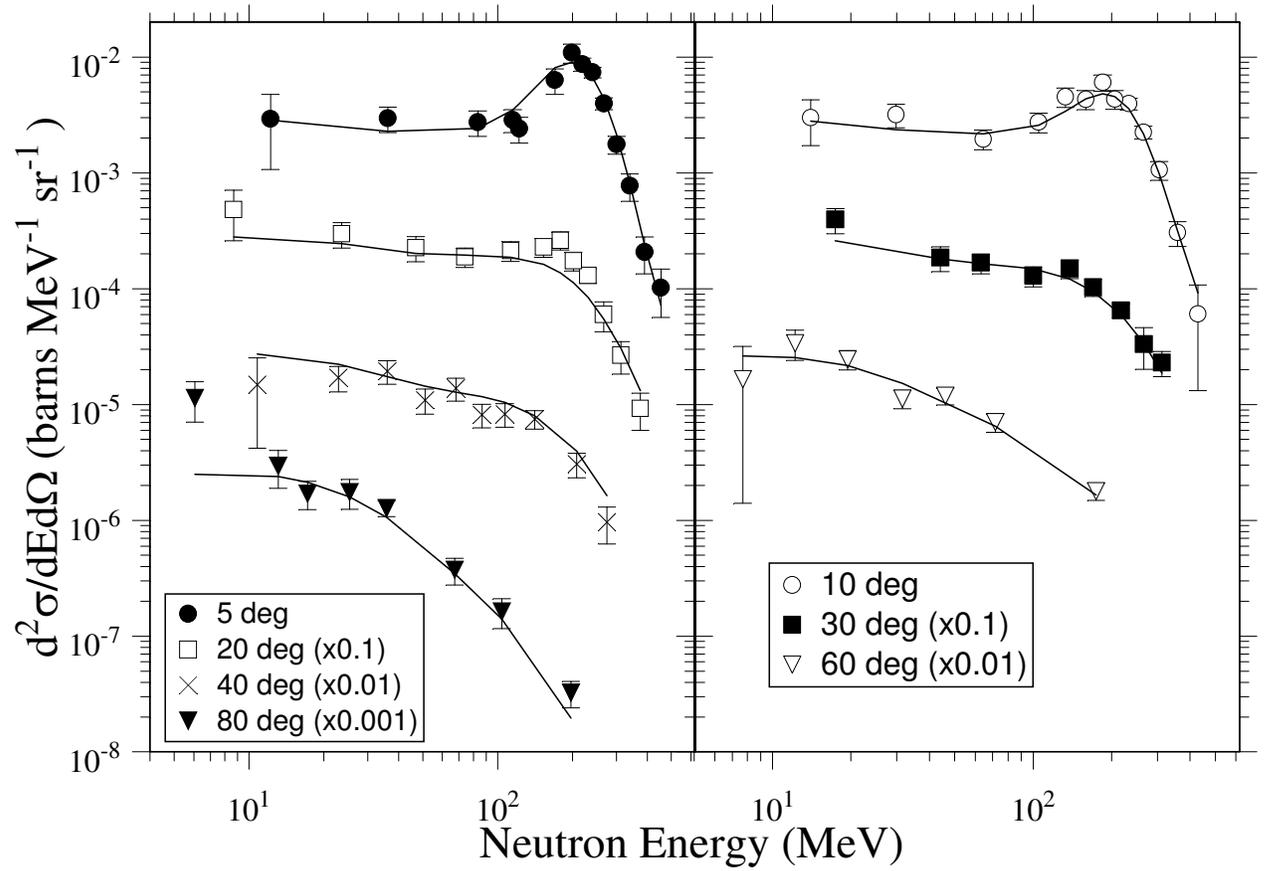
Fig. 27. Angular distribution from the 400 MeV/nucleon Kr systems for $E_n > 10$ MeV. The lines show a fit to the data using Eqn. 5.

Fig. 28. Angular distribution from the 400 MeV/nucleon Xe systems for $E_n > 10$ MeV. The lines show a fit to the data using Eqn. 5.

Fig. 29. Angular distribution from the 600 MeV/nucleon Si systems for $E_n > 10$ MeV. The lines show a fit to the data using Eqn. 5.

Fig. 30. Total cross sections for neutrons above 10 MeV and angles between 0 and 180 degrees, as a function of a parameter that is proportional to the geometric cross sections. The lines indicate fits to the data using Eqn. 6.

TABLE CAPTIONS

Table I

Target species and thickness (g/cm^2) used with the indicated beams

Table II

Neutron detector information. The uncertainty in the solid angle is reported as a

percentage.

Table III

Systematic uncertainties as a function of detector number, expressed as a percentage.

Adding the individual uncertainties in quadrature yields the total systematic uncertainty

listed in column 7.

Table IV

Parameters from moving source fits to the indicated systems. The first part of the table

contains the parameters of the projectile fragmentation source, and the second part

contains the parameters from the two Maxwellian sources (see Eqns. 1 and 4).

Table V

Parameters from fits to the indicated angular distributions using Eqn. 5.

Table VI

Total cross sections for the indicated systems. Columns 3 – 5 show the integrated cross sections from 0 to 90 degrees. Column six shows the deduced total cross sections from 0 to 180 degrees.

Fig. 1. A schematic view of the experimental arrangement used for the measurements (not to scale).

Fig. 2. The fraction of neutron flux transmitted from the target to the neutron detector as a function of neutron energy. Plots are shown for the four cases indicated in the legend.
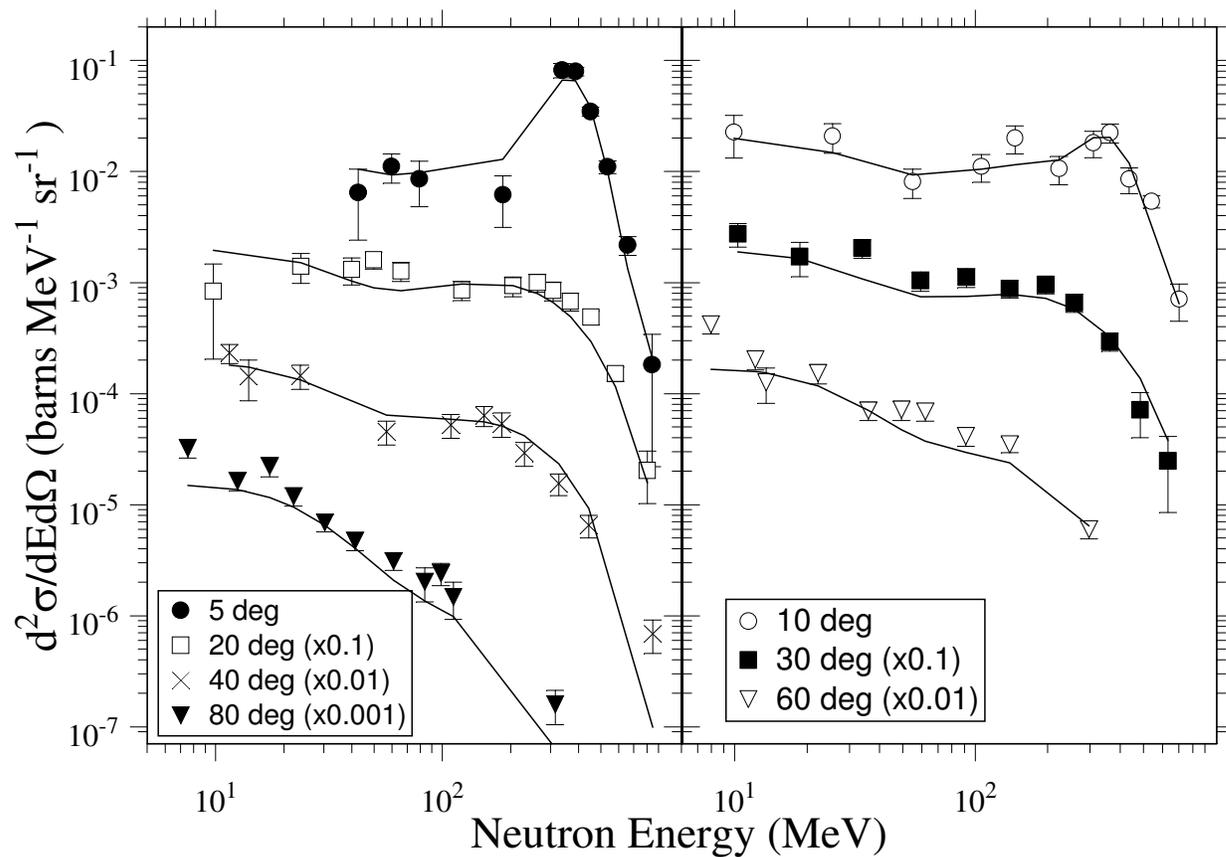
Fig. 3. Double-differential spectra from 230 MeV/nucleon He interacting in an Al target. The spectra at each laboratory angle are offset by the indicated factors of 10. The lines come from a moving-source fit described in the text.
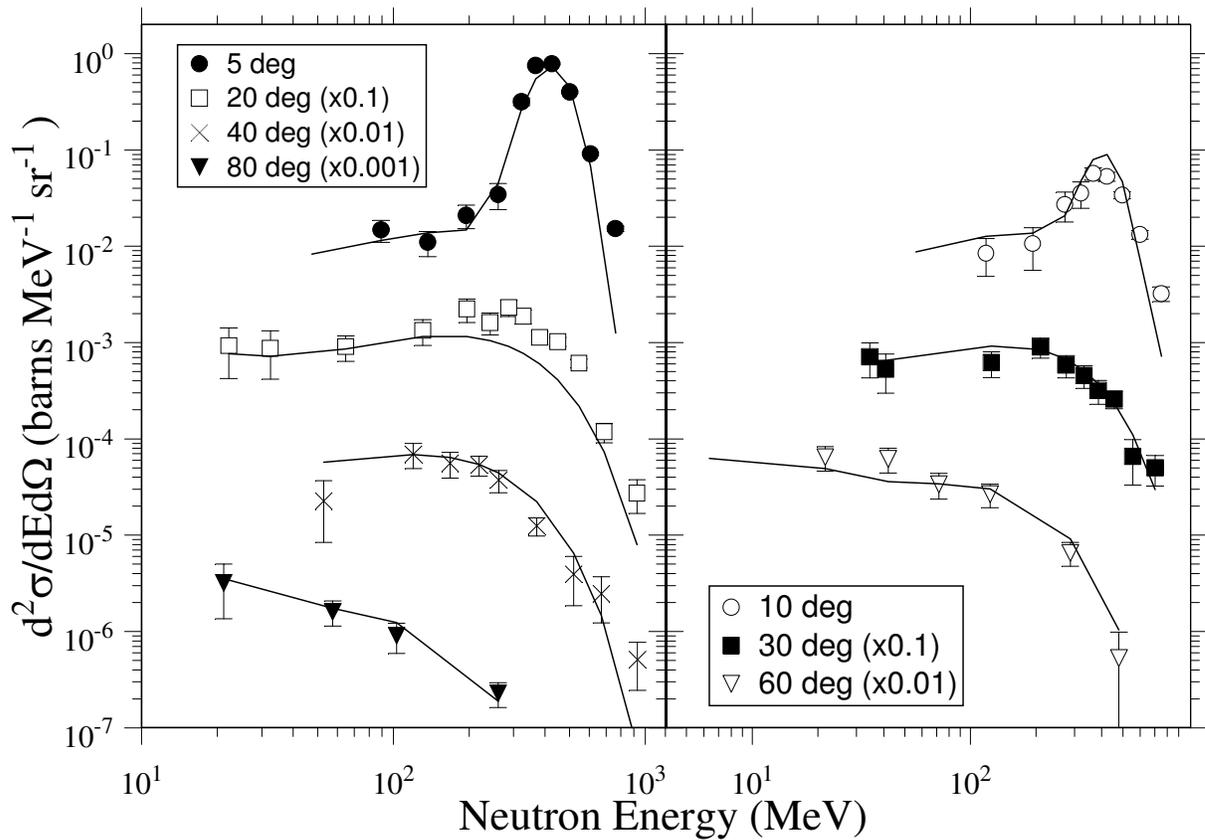
Fig. 4. Double-differential spectra from 230 MeV/nucleon He interacting in a Cu target. The spectra at each laboratory angle are offset by the indicated factors of 10. The lines come from a moving-source fit described in the text.
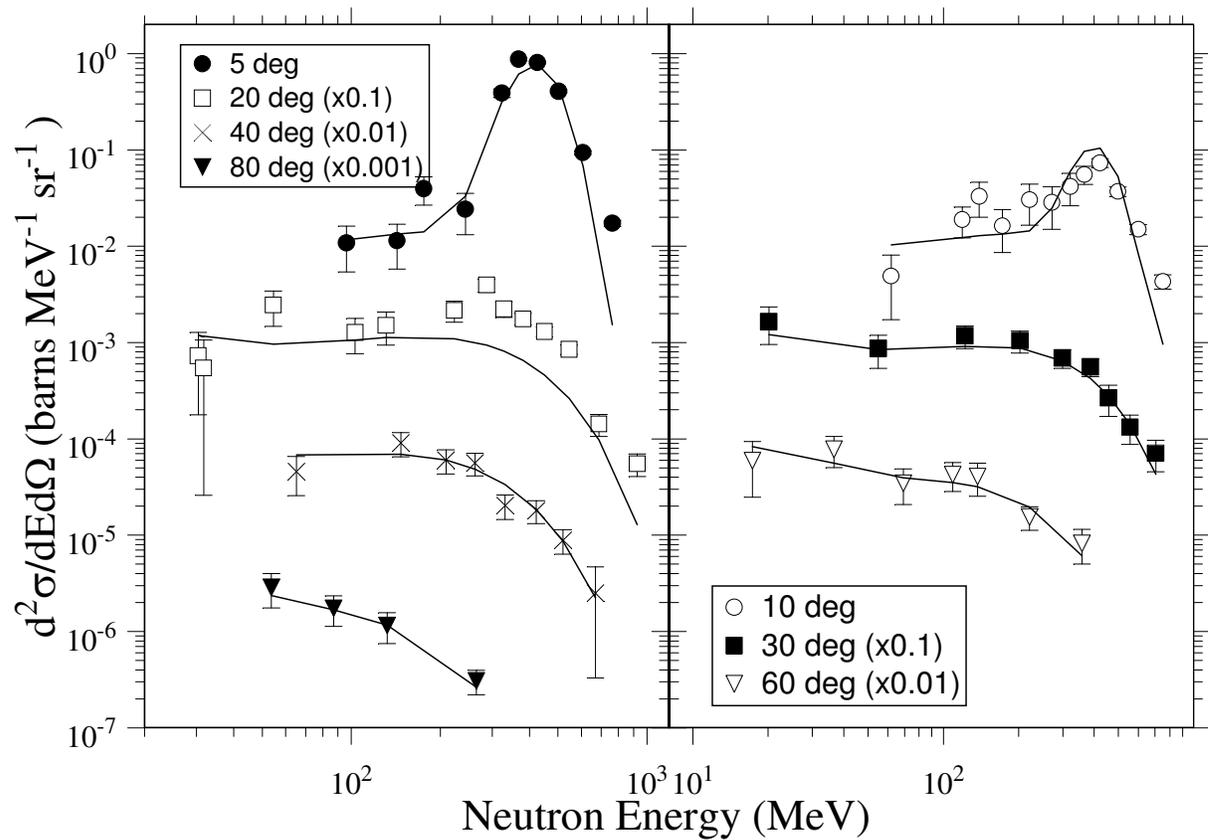
Fig. 5. Double-differential spectra from 400 MeV/nucleon N interacting in a C target. The spectra at each laboratory angle are offset by the indicated factors of 10. The lines come from a moving-source fit described in the text.

Fig. 6. Double-differential spectra from 400 MeV/nucleon N interacting in a Cu target. The spectra at each laboratory angle are offset by the indicated factors of 10. The lines come from a moving-source fit described in the text.
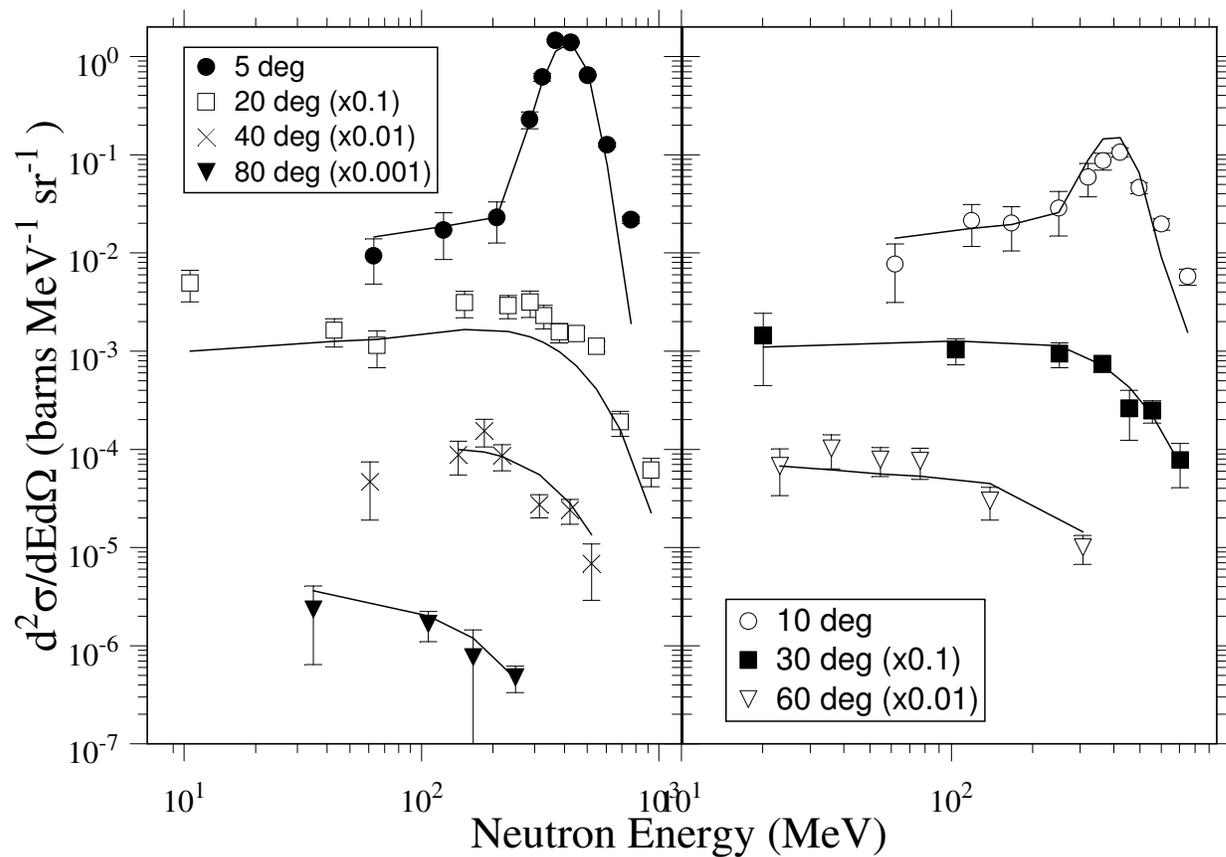
Fig. 7. Double-differential spectra from 400 MeV/nucleon Kr interacting in a Li target. The spectra at each laboratory angle are offset by the indicated factors of 10. The lines come from a moving-source fit described in the text.
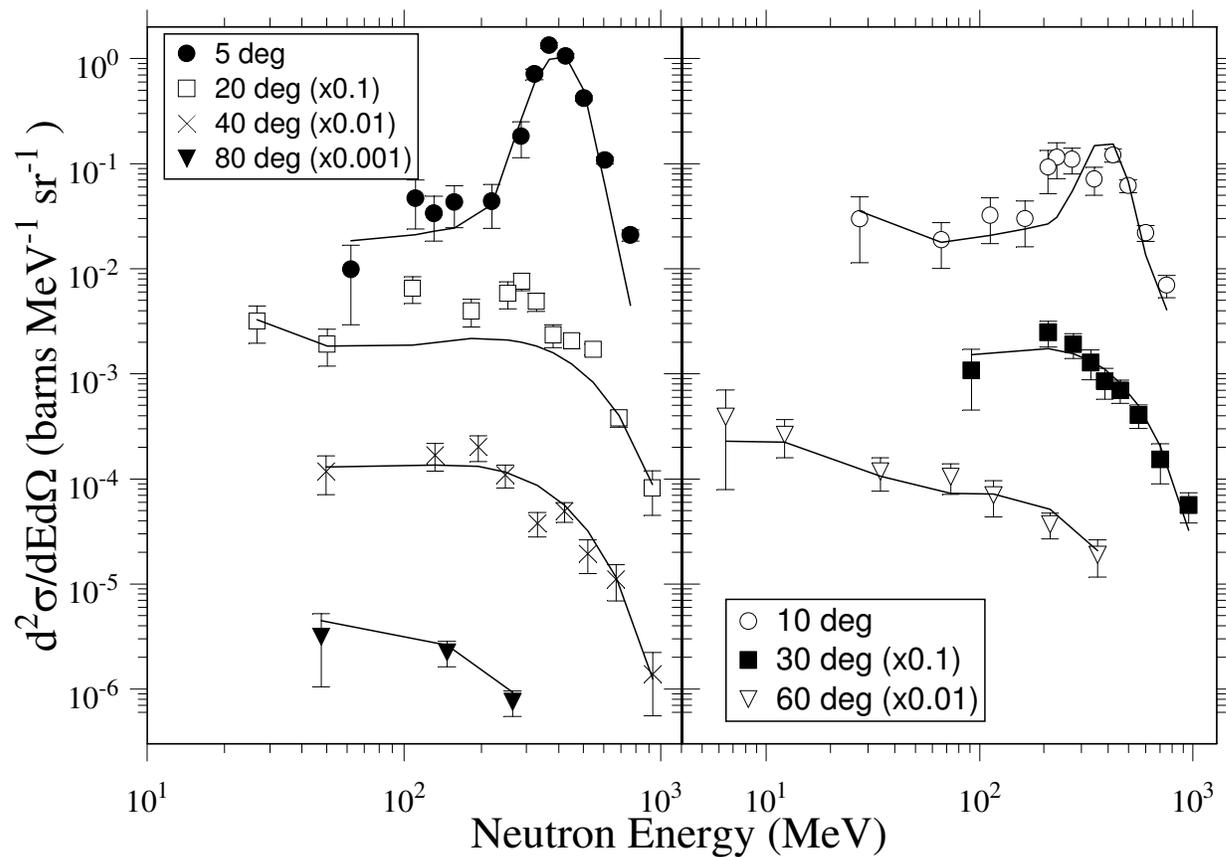
Fig. 8. Double-differential spectra from 400 MeV/nucleon Kr interacting in a C target. The spectra at each laboratory angle are offset by the indicated factors of 10. The lines come from a moving-source fit described in the text.

Fig. 9. Double-differential spectra from 400 MeV/nucleon Kr interacting in a

CH$_2$ target. The spectra at each laboratory angle are offset by the indicated factors of 10.

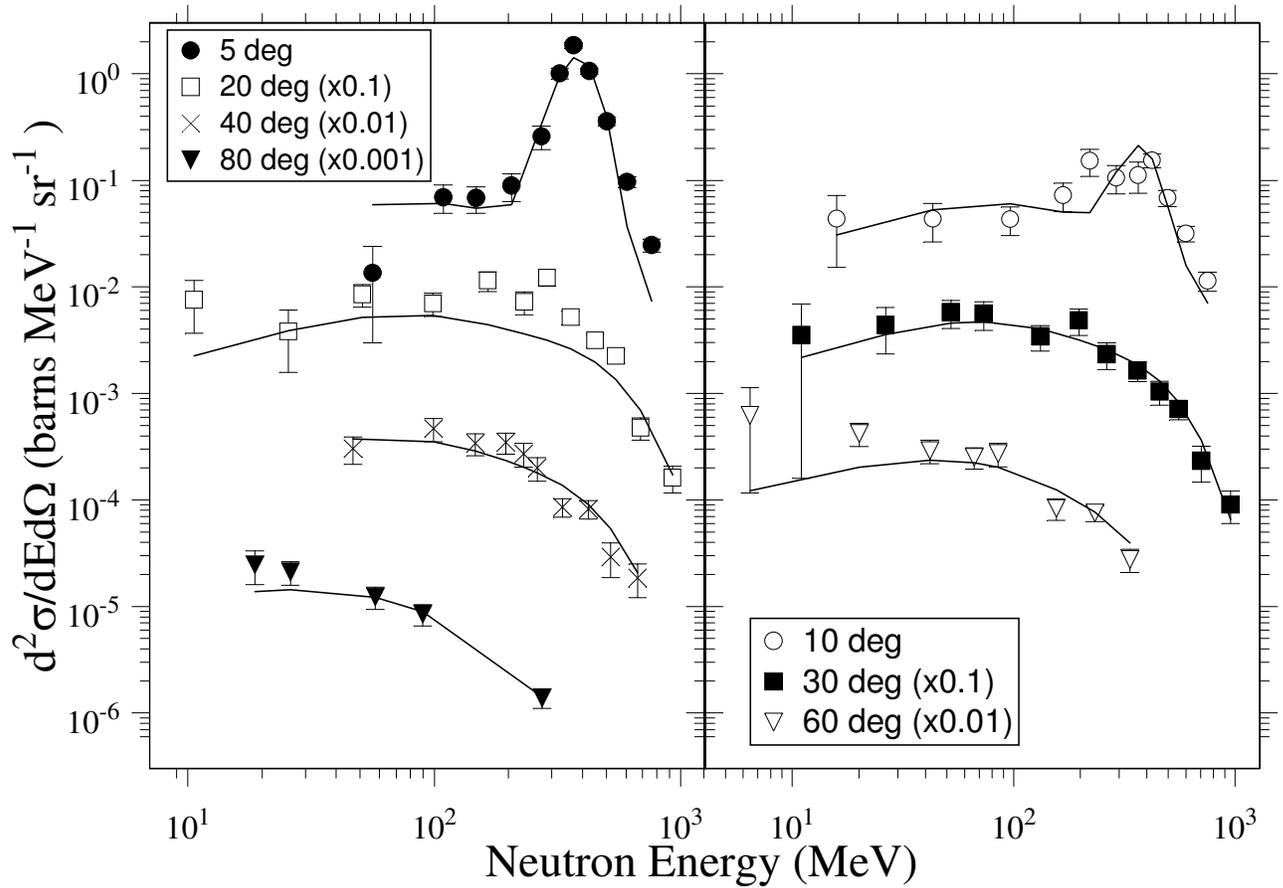The lines come from a moving-source fit described in the text.

Fig. 10. Double-differential spectra from 400 MeV/nucleon Kr interacting in an Al target. The spectra at each laboratory angle are offset by the indicated factors of 10. The lines come from a moving-source fit described in the text.
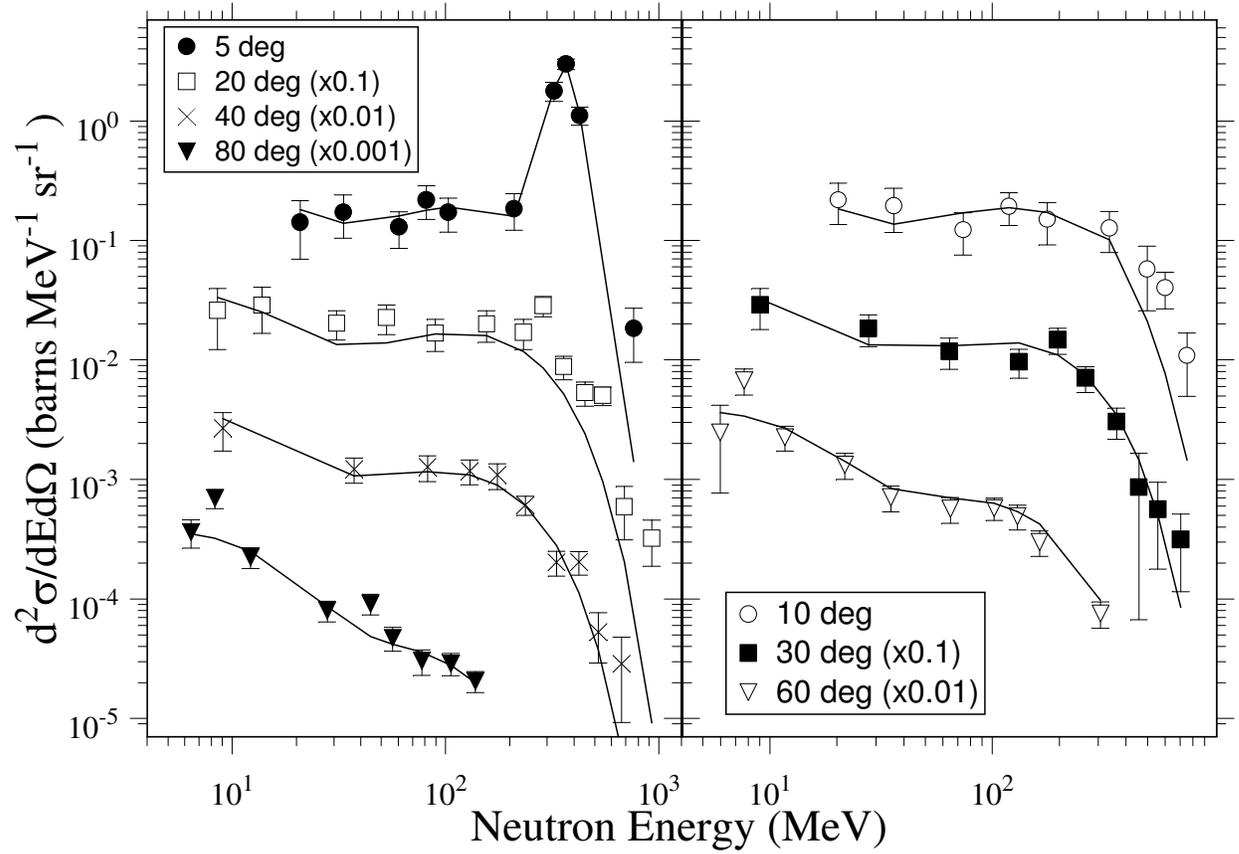
Fig. 11. Double-differential spectra from 400 MeV/nucleon Kr interacting in a Cu target. The spectra at each laboratory angle are offset by the indicated factors of 10. The lines come from a moving-source fit described in the text.

Fig. 12. Double-differential spectra from 400 MeV/nucleon Kr interacting in a Pb target. The spectra at each laboratory angle are offset by the indicated factors of 10. The lines come from a moving-source fit described in the text.
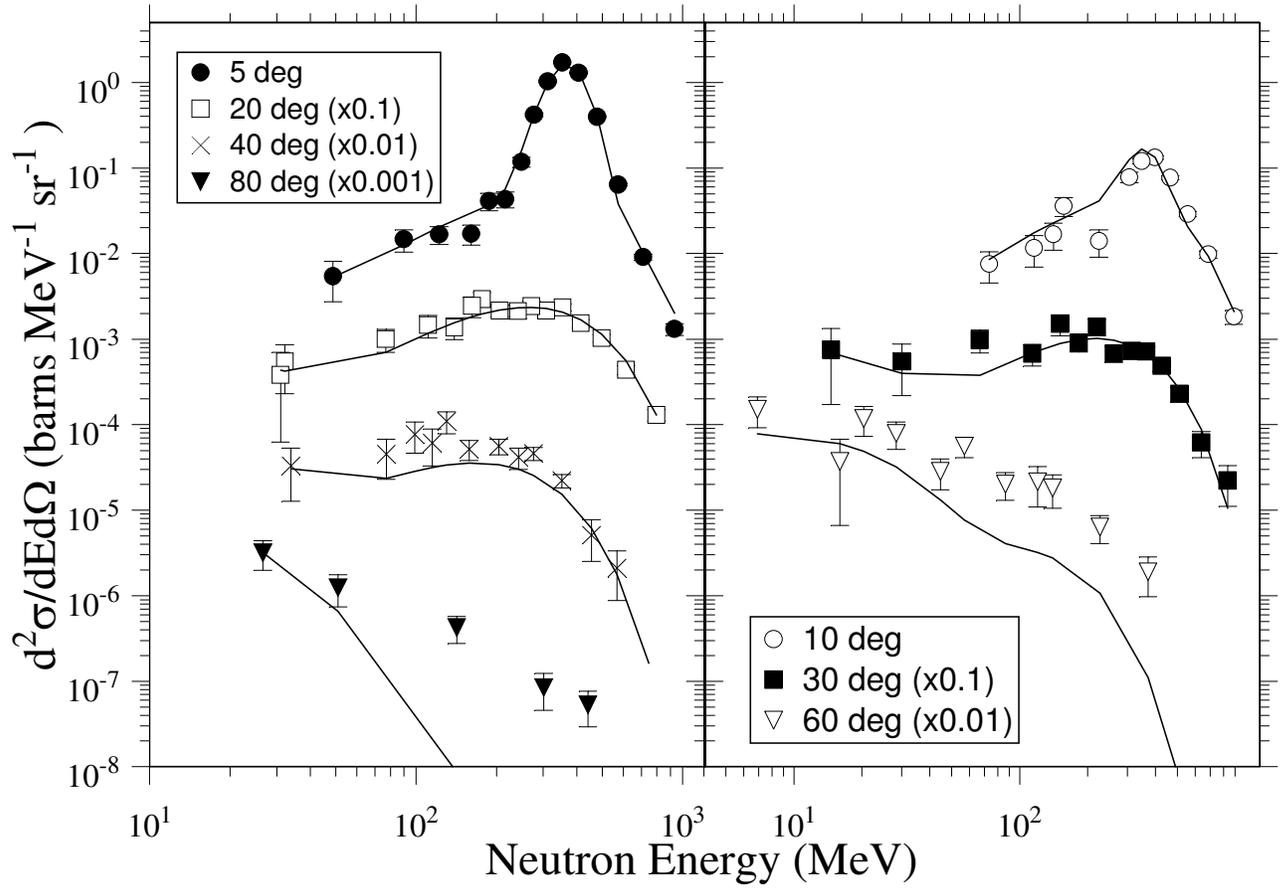
Fig. 13. Double-differential spectra from 400 MeV/nucleon Xe interacting in a Li target. The spectra at each laboratory angle are offset by the indicated factors of 10. The lines come from a moving-source fit described in the text.
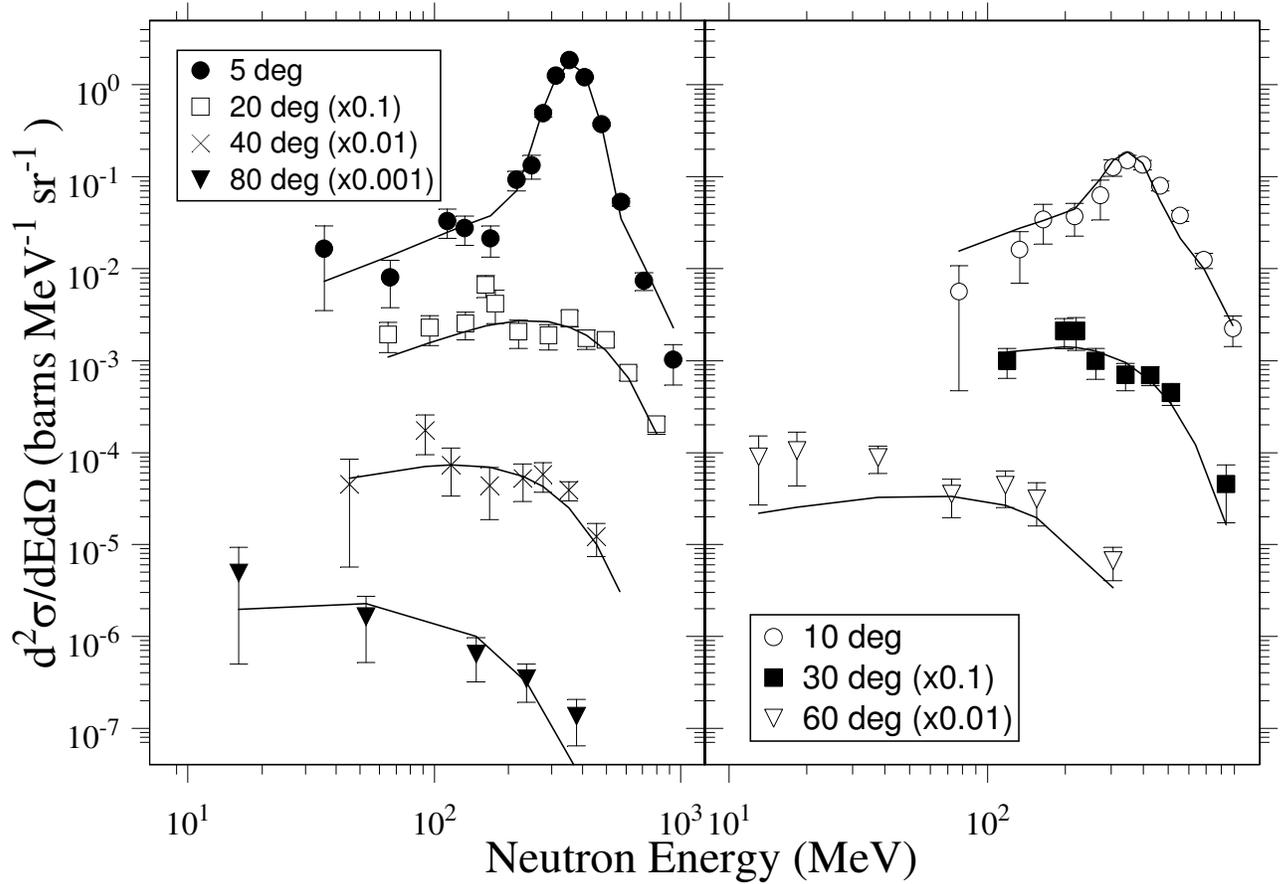
Fig. 14. Double-differential spectra from 400 MeV/nucleon Xe interacting in a C target. The spectra at each laboratory angle are offset by the indicated factors of 10. The lines come from a moving-source fit described in the text.

Fig. 15. Double-differential spectra from 400 MeV/nucleon Xe interacting in a CH$_2$ target. The spectra at each laboratory angle are offset by the indicated factors of 10. The lines come from a moving-source fit described in the text.
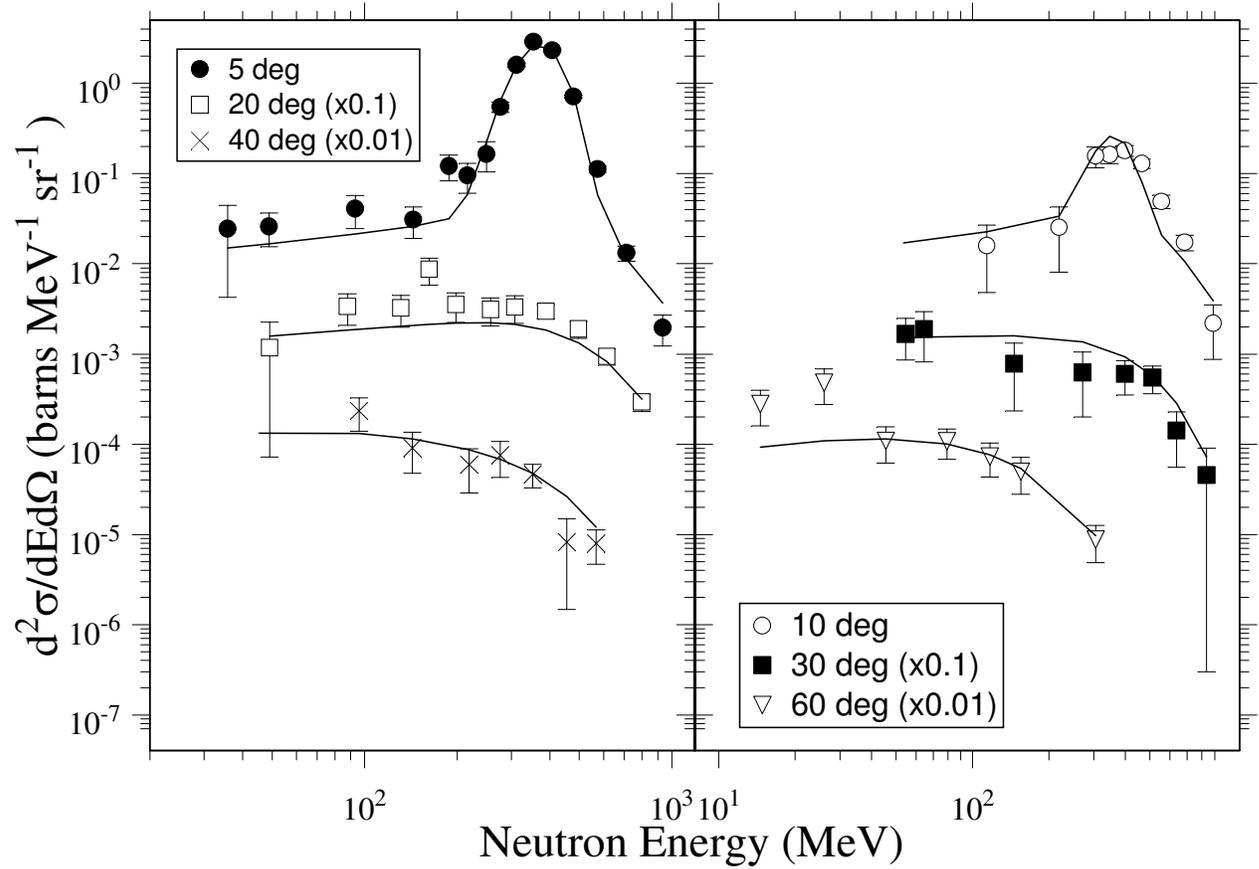
Fig. 16. Double-differential spectra from 400 MeV/nucleon Xe interacting in an
Al target. The spectra at each laboratory angle are offset by the indicated factors of 10.
The lines come from a moving-source fit described in the text.

Fig. 17. Double-differential spectra from 400 MeV/nucleon Xe interacting in a Cu target. The spectra at each laboratory angle are offset by the indicated factors of 10. The lines come from a moving-source fit described in the text.
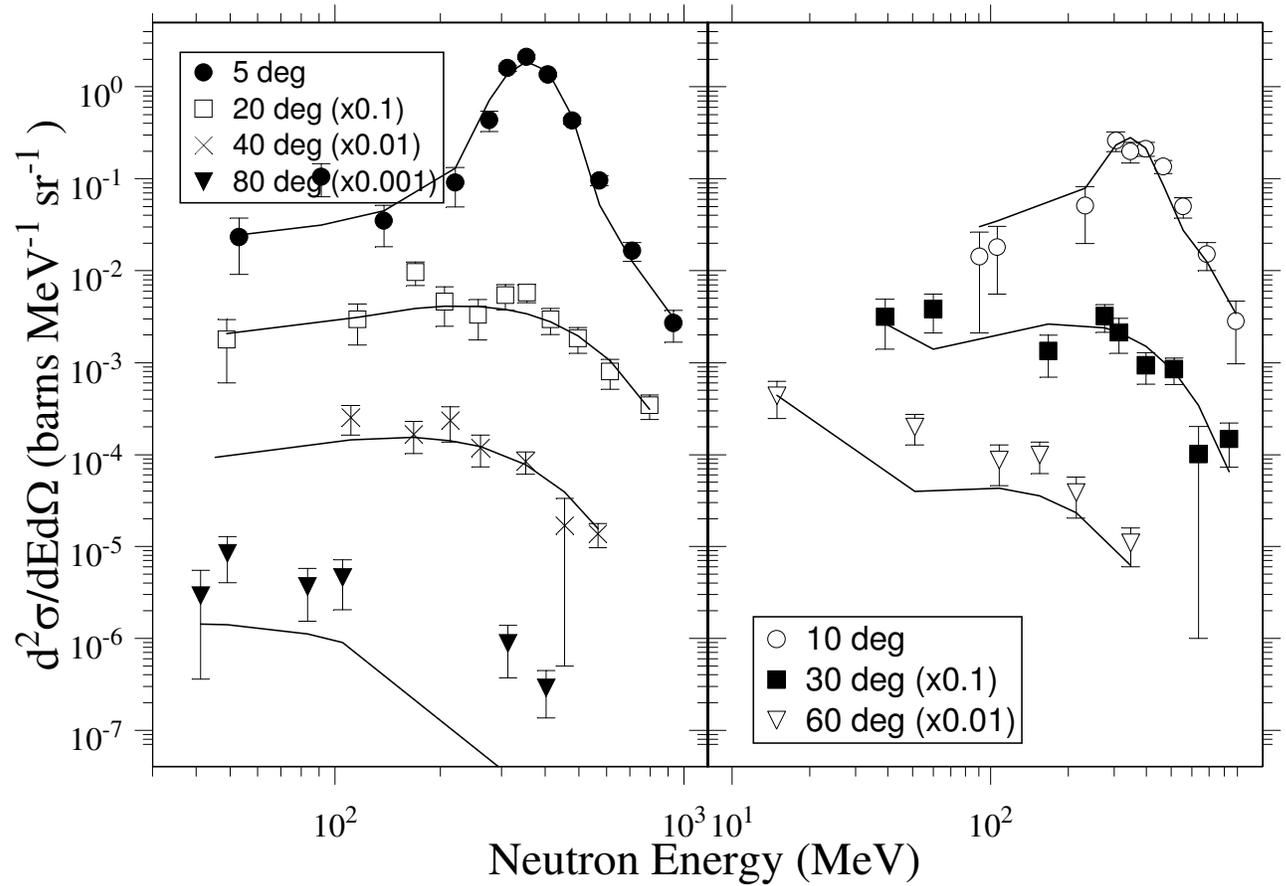
Fig. 18. Double-differential spectra from 400 MeV/nucleon Xe interacting in a Pb target. The spectra at each laboratory angle are offset by the indicated factors of 10. The lines come from a moving-source fit described in the text.

Fig. 19. Double-differential spectra from 500 MeV/nucleon Fe interacting in a Li target. The spectra at each laboratory angle are offset by the indicated factors of 10. The lines come from a moving-source fit described in the text.
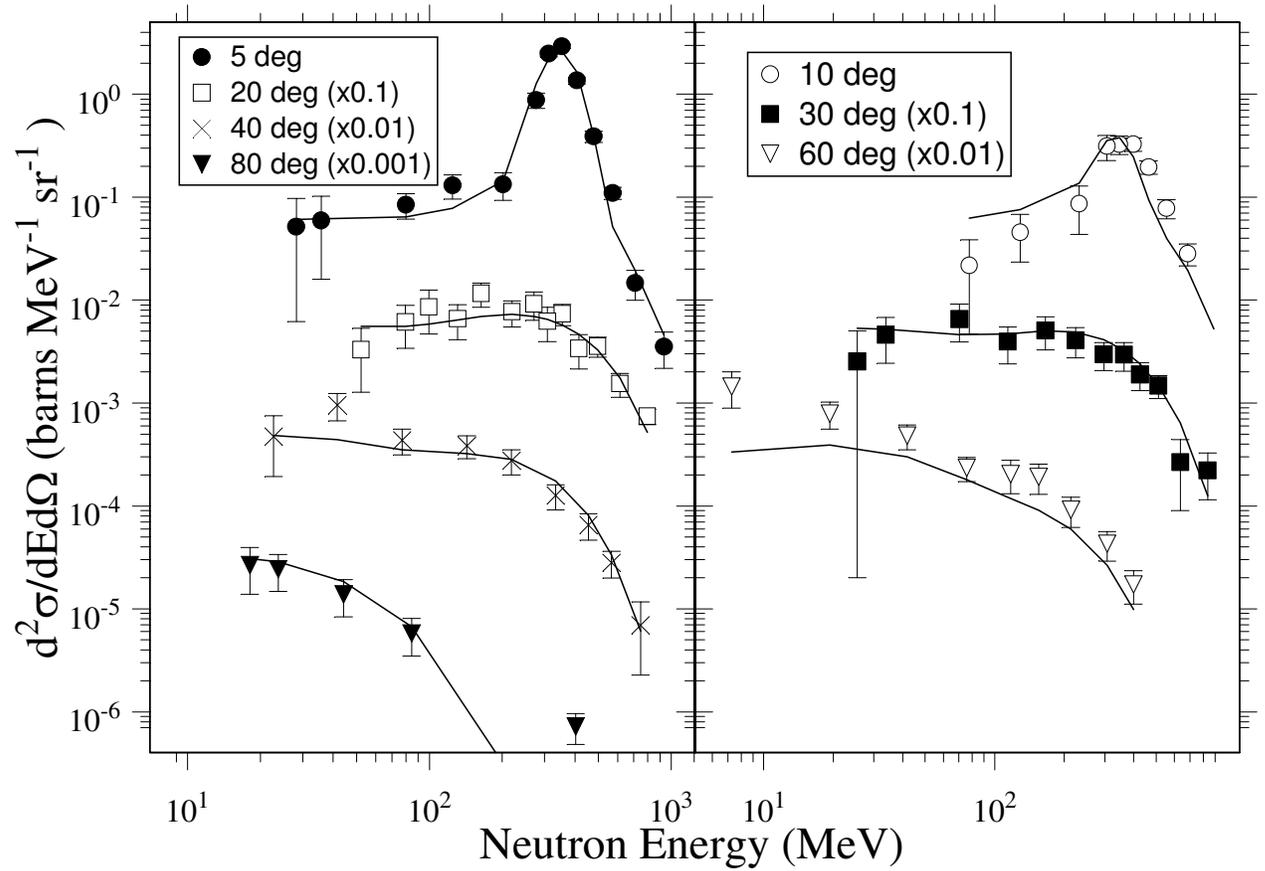
Fig. 20. Double-differential spectra from 500 MeV/nucleon Fe interacting in a CH$_2$ target. The spectra at each laboratory angle are offset by the indicated factors of 10.

Fig. 21. Double-differential spectra from 500 MeV/nucleon Fe interacting in an Al target. The spectra at each laboratory angle are offset by the indicated factors of 10. The lines come from a moving-source fit described in the text.
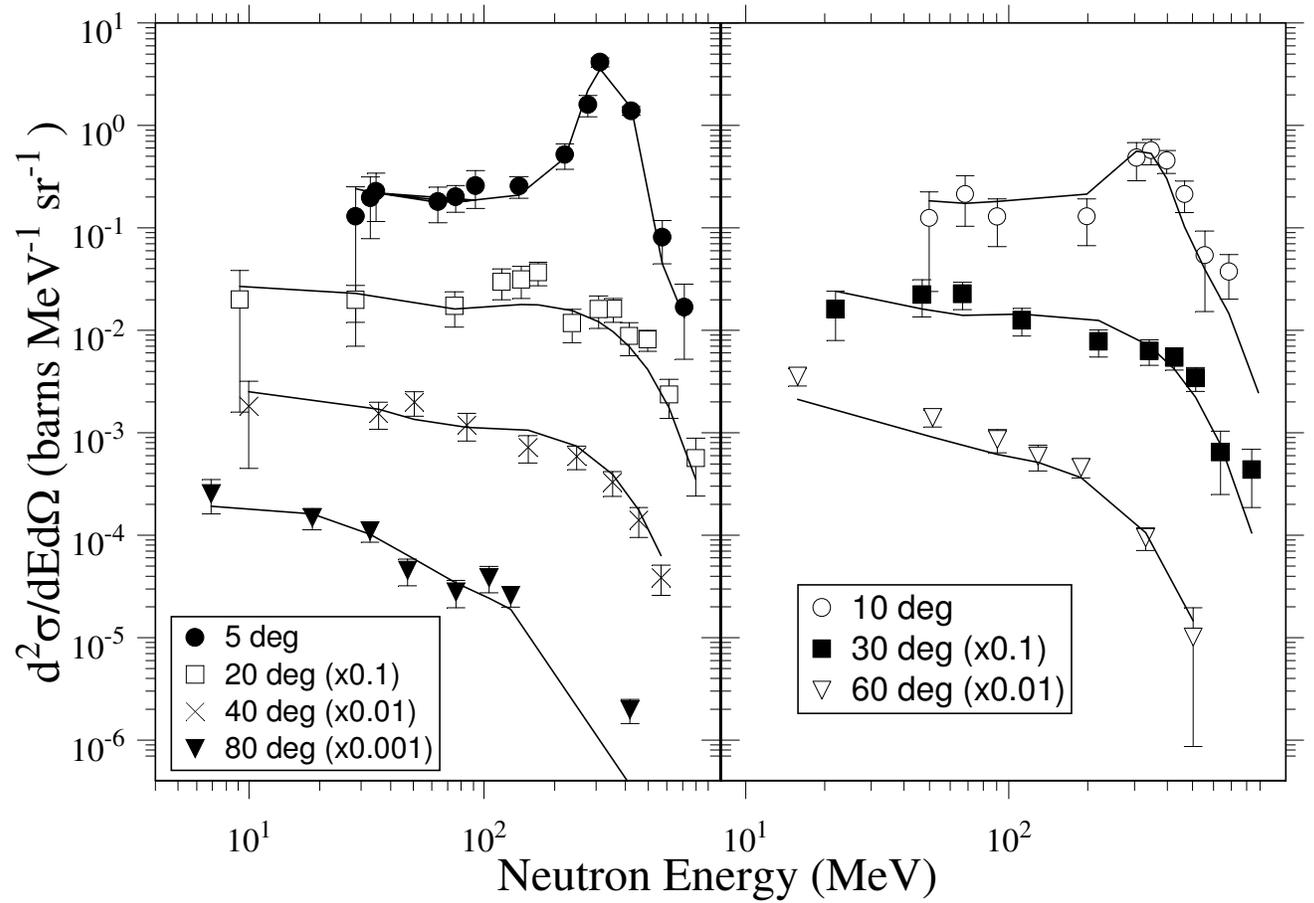
Fig. 22. Double-differential spectra from 600 MeV/nucleon Si interacting in a C target. The spectra at each laboratory angle are offset by the indicated factors of 10. The lines come from a moving-source fit described in the text.
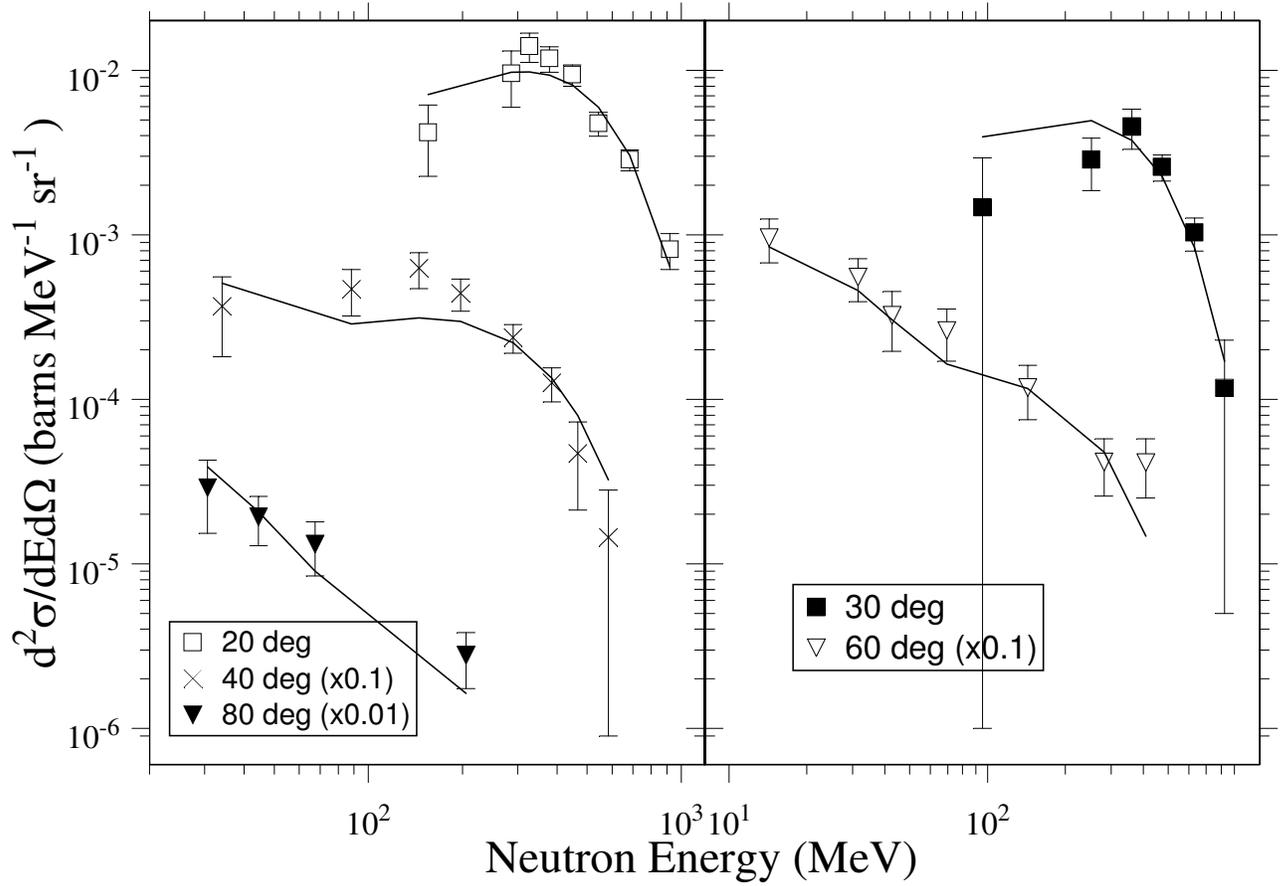
Fig. 23. Double-differential spectra from 600 MeV/nucleon Si interacting in a Cu target. The spectra at each laboratory angle are offset by the indicated factors of 10. The lines come from a moving-source fit described in the text.

Fig. 24. Double-differential spectra from 600 MeV/nucleon Si interacting in a Pb target. The spectra at each laboratory angle are offset by the indicated factors of 10. The lines come from a moving-source fit described in the text.
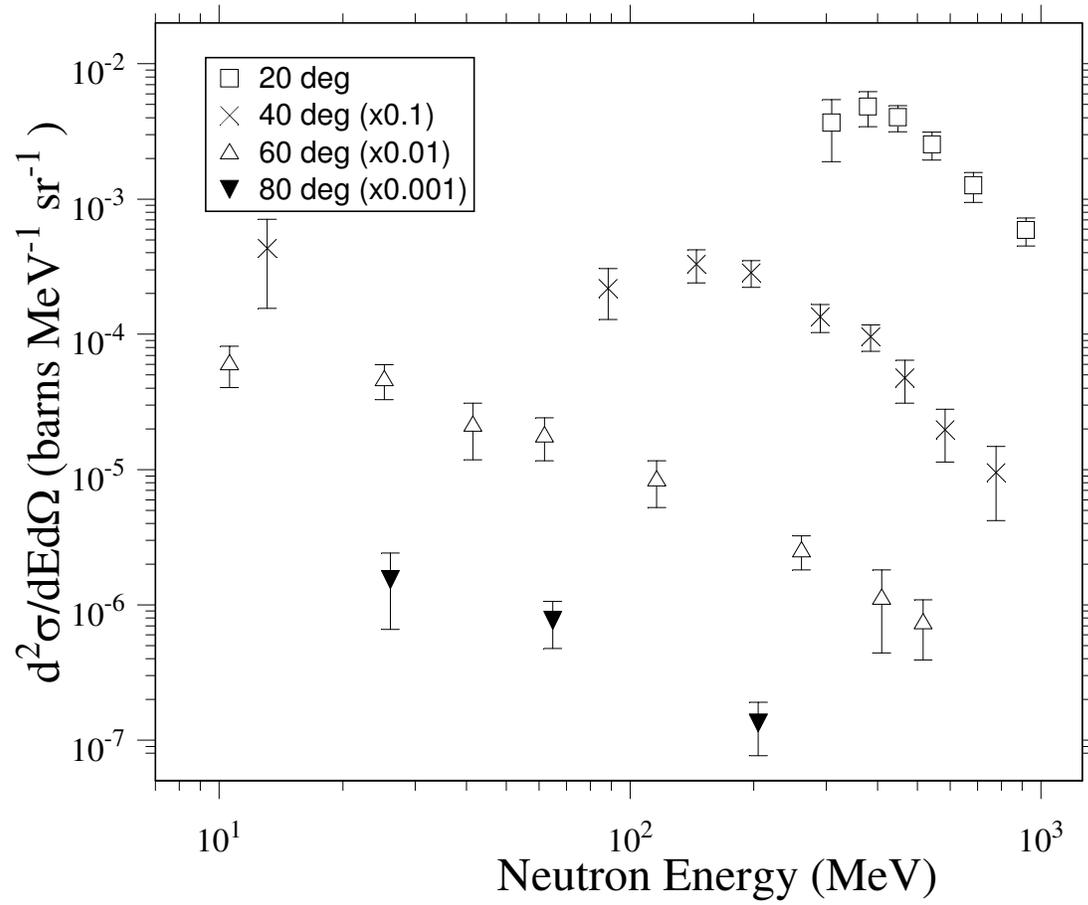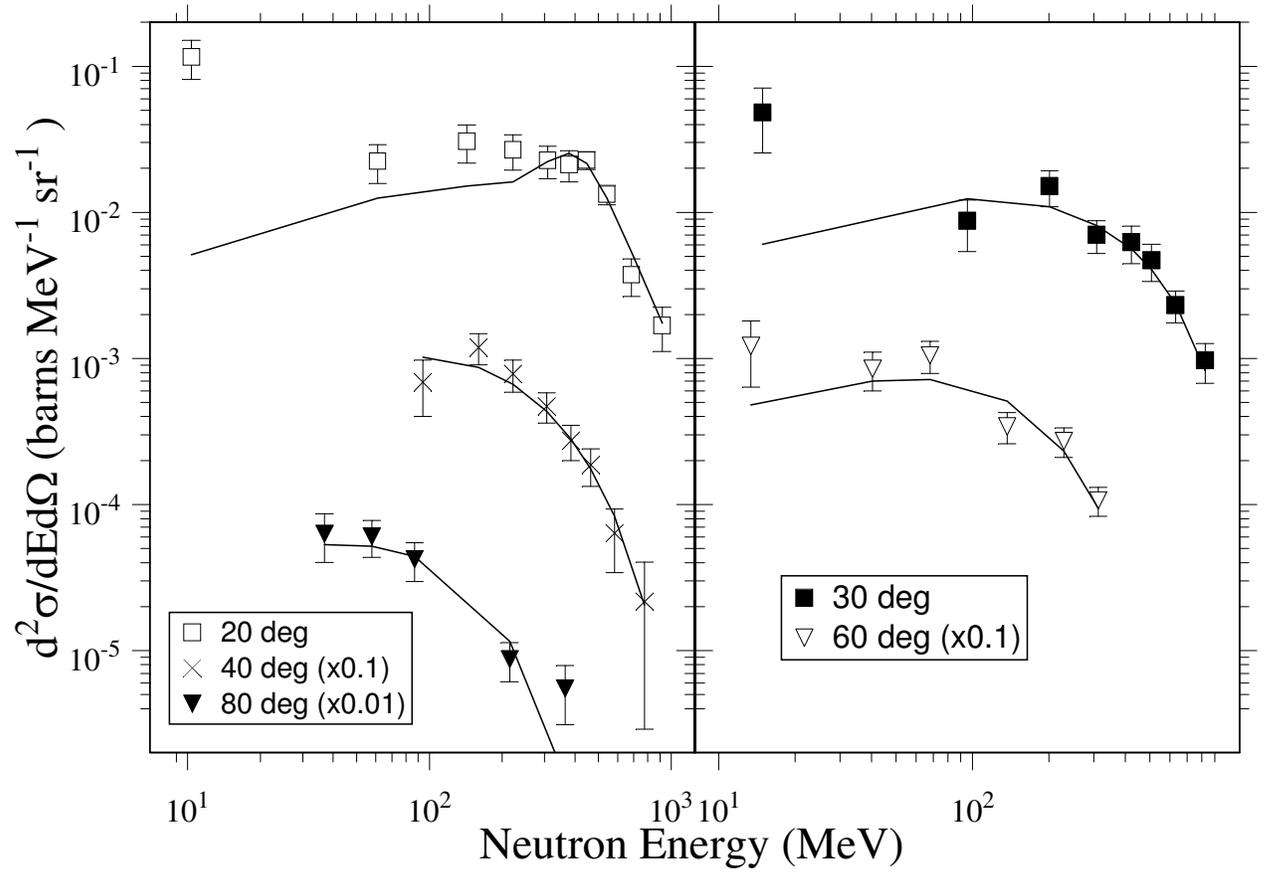
Fig. 25. Angular distribution from the 230 MeV/nucleon He systems for $E_n > 10$ MeV. The lines show a fit to the data using Eqn. 5.

Fig. 26. Angular distribution from the 400 MeV/nucleon N systems for $E_n > 10$ MeV. The lines show a fit to the data using Eqn. 5.

Fig. 27. Angular distribution from the 400 MeV/nucleon Kr systems for $E_n > 10$ MeV. The lines show a fit to the data using Eqn. 5.

Fig. 28. Angular distribution from the 400 MeV/nucleon Xe systems for $E_n > 10$

MeV. The lines show a fit to the data using Eqn. 5.

Fig. 29. Angular distribution from the 600 MeV/nucleon Si systems for $E_n > 10$ MeV. The lines show a fit to the data using Eqn. 5.

Fig. 30. Total cross sections for neutrons above 10 MeV and angles between 0 and 180 degrees, as a function of a parameter that is proportional to the geometric cross sections. The lines indicate fits to the data using Eqn. 6.

Table I

Target species and thickness (g/cm^2) used with the indicated beams

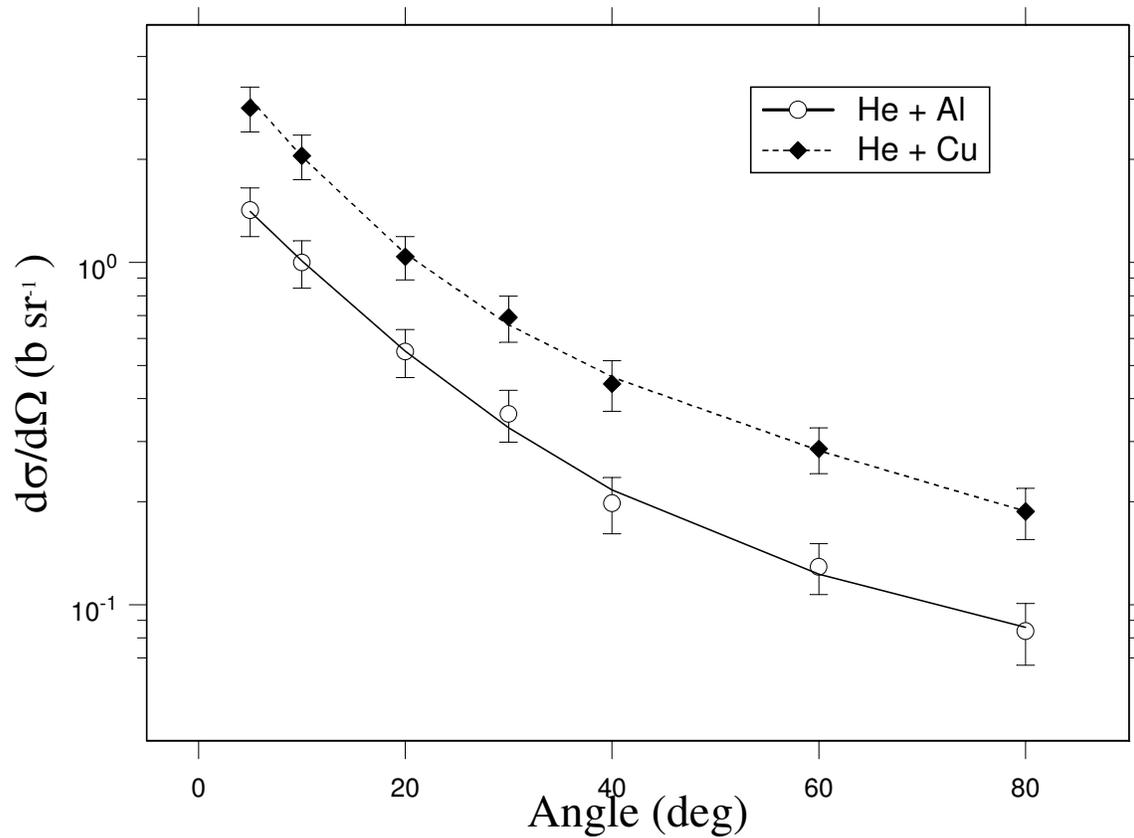| Beam (energy) (MeV/nucleon)	Target	Thickness (g/cm^2)
He (230)	Al	5.40 (2.0 cm)
	Cu	5.38 (0.6 cm)
N (400)	C	1.78 (1.0 cm)
	Cu	2.69 (0.3 cm)
Si (600)	C	1.80 (1.0 cm)
	Cu	3.58 (0.4 cm)
	Pb	4.54 (0.4 cm)
Fe (500)	Li	0.903 (1.7 cm)
	CH$_2$	0.957 (1.05 cm)
	Al	1.285 (0.476 cm)
Kr (400)	Li	0.47 (0.885 cm)
	C	0.55 (0.3 cm)
	CH$_2$	0.46 (0.5 cm)
	Al	0.54 (0.2 cm)
	Cu	0.90 (0.1 cm)
	Pb	1.02 (0.09 cm)
Xe (400)	Li	0.48 (0.9 cm)
	C	0.27 (0.15 cm)
	CH$_2$	0.20 (0.22 cm)
	Al	0.26 (0.095 cm)
	Cu	0.45 (0.05 cm)
	Pb	0.57 (0.05 cm)

Table II

Neutron detector information. The uncertainty in the solid angle is reported as a

percentage.

Detector	Flight Path Length (cm)	Lab angle (deg)	Solid angle (msr)
N1	506	5	0.494 ± 5.0%
N2	506	10	0.494 ± 5.0%
N3	456	20	0.608 ± 5.6%
N4	456	30	0.608 ± 5.6%
N5	406	40	0.767 ± 6.2%
N6	356	60	0.998 ± 7.1%
N7	306	80	1.35 ± 8.3%

Table III

Systematic uncertainties as a function of detector number, expressed as a percentage.

Adding the individual uncertainties in quadrature yields the total systematic uncertainty

listed in column 7.

Detector number	Detection Efficiency	Flux Attenuation	Solid Angle	QDC calibration	Beam Integration	Total
N1	10	7	5.0	5.2	4	14.7
N2	10	7	5.0	5.4	4	14.8
N3	10	7	5.6	3.8	4	14.5
N4	10	7	5.6	6.3	4	15.4
N5	10	7	6.2	9.1	4	16.9
N6	10	7	7.1	3.8	4	15.2
N7	10	7	8.3	7.9	4	17.2

Table IV

Parameters from moving source fits to the indicated systems. The first part of the table contains the parameters of the projectile fragmentation source, and the second part contains the parameters from the two Maxwellian sources (see Eqns. 1 and 4).

Beam (AMeV)	Target	Projectile fragmentation parameters		
		N_1	σ (MeV/c)	β
230 He	Al	$(1.67 \pm 0.18) \times 10^{-8}$	75.9 ± 4.0	0.559 ± 0.004
230 He	Cu	$(5.1 \pm 0.6) \times 10^{-8}$	68.8 ± 3.0	0.553 ± 0.004
400 N	C	$(8.7 \pm 0.8) \times 10^{-8}$	67.6 ± 2.4	0.696 ± 0.002
400 N	Cu	$(1.22 \pm 0.17) \times 10^{-7}$	78.2 ± 4.1	0.690 ± 0.004
400 Kr	Li	$(1.61 \pm 0.04) \times 10^{-6}$	71.6 ± 0.6	0.724 ± 0.001
400 Kr	C	$(1.66 \pm 0.06) \times 10^{-6}$	72.9 ± 0.8	0.721 ± 0.001
400 Kr	CH_2	$(3.23 \pm 0.10) \times 10^{-6}$	69.0 ± 0.7	0.719 ± 0.001
400 Kr	Al	$(2.31 \pm 0.15) \times 10^{-6}$	72.7 ± 1.4	0.712 ± 0.001
400 Kr	Cu	$(3.23 \pm 0.28) \times 10^{-6}$	68.9 ± 1.9	0.702 ± 0.002
400 Kr	Pb	$(1.63 \pm 0.79) \times 10^{-5}$	44.5 ± 6	0.694 ± 0.003
400 Xe	Li	$(4.43 \pm 0.08) \times 10^{-6}$	60.8 ± 0.4	0.6957 ± 0.0003
400 Xe	C	$(4.58 \pm 0.18) \times 10^{-6}$	61.2 ± 0.8	0.6915 ± 0.0007
400 Xe	CH_2	$(7.30 \pm 0.27) \times 10^{-6}$	62.1 ± 0.8	0.698 ± 0.001
400 Xe	Al	$(4.37 \pm 0.32) \times 10^{-6}$	66.4 ± 1.8	0.690 ± 0.0013
400 Xe	Cu	$(6.27 \pm 0.52) \times 10^{-6}$	64.1 ± 1.5	0.682 ± 0.0015
400 Xe	Pb	$(9.54 \pm 1.88) \times 10^{-6}$	62.6 ± 4.0	0.676 ± 0.002
500 Fe	Li	$(2.25 \pm 0.77) \times 10^{-8}$	203 ± 17	0.716 ± 0.023
500 Fe	Al	$(8.1 \pm 44) \times 10^{-6}$	101 ± 101	0.74 ± 0.10
600 Si	C	$(1.31 \pm 0.06) \times 10^{-7}$	91.3 ± 1.4	0.768 ± 0.001
600 Si	Cu	$(1.67 \pm 0.11) \times 10^{-7}$	106 ± 3	0.763 ± 0.002
600 Si	Pb	$(2.45 \pm 0.31) \times 10^{-7}$	116 ± 6	0.751 ± 0.003

Beam (AMeV)	Tgt	Pre-equilibrium source			Equilibrium Source		
		N	T (MeV)	β	N	T (MeV)	β
230 He	Al	0.88 ± 0.05	44.7 ± 1.8	0.311 ± 0.013	0.87 ± 0.09	14.8 ± 2.0	0.00 ± 0.13
230 He	Cu	2.19 ± 0.14	49.0 ± 1.9	0.250 ± 0.014	2.14 ± 0.30	7.9 ± 1.0	0.027 ± 0.012
400 N	C	1.83 ± 0.09	62.8 ± 2.5	0.516 ± 0.010	1.24 ± 0.17	21.7 ± 2.3	0.007 ± 0.024
400 N	Cu	7.2 ± 0.3	73.0 ± 2.4	0.408 ± 0.013	4.7 ± 0.4	13.0 ± 1.1	0.033 ± 0.012
400 Kr	Li	8.8 ± 0.4	76 ± 4	0.419 ± 0.020	1.2 ± 0.5	10.4 ± 8.8	0.044 ± 0.068
400 Kr	C	9.7 ± 0.8	82.7 ± 5.5	0.418 ± 0.020	2.1 ± 1.8	12.9 ± 11.5	0.079 ± 0.133
400 Kr	CH_2	14.1 ± 0.8	84 ± 7	0.43 ± 0.02	1.4 ± 0.8	14 ± 12	0.104 ± 0.08
400 Kr	Al	22.3 ± 1.0	101 ± 8	0.438 ± 0.019	4.7 ± 1.3	9.4 ± 3.8	0.098 ± 0.071

400 Kr	Cu	34.2 ± 1.5	107 ± 12	0.44 ± 0.02	14.8 ± 1.7	36.7 ± 7.4	0.23 ± 0.05
400 Kr	Pb	129 ± 5	69 ± 3	0.327 ± 0.015	72 ± 7	8.0 ± 1.1	0.0 ± 0.02
400 Xe	Li	10.3 ± 0.3	48.6 ± 1.5	0.610 ± 0.004	2.4 ± 0.4	12.6 ± 1.6	0.0085 ± 0.015
400 Xe	C	12.0 ± 0.8	52 ± 2	0.600 ± 0.011	4.3 ± 0.8	70 ± 6	0.18 ± 0.08
400 Xe	CH$_2$	14.0 ± 0.9	77 ± 13	0.573 ± 0.085	18 ± 3	70 ± 18	0.0 ± 0.063
400 Xe	Al	25.1 ± 1.8	70 ± 5	0.538 ± 0.017	40 ± 37	2.9 ± 0.4	0.132 ± 0.015
400 Xe	Cu	48 ± 3	74 ± 4	0.514 ± 0.014	17.3 ± 3.2	23 ± 5	0.074 ± 0.035
400 Xe	Pb	142 ± 9	78 ± 3	0.396 ± 0.019	67 ± 10	14.9 ± 2.7	0.044 ± 0.025
500 Fe	Li	4.5 ± 0.5	83 ± 6	0.47 ± 0.03	3.0 ± 0.5	14 ± 4	0.022 ± 0.046
500 Fe	Al	8.0 ± 0.9	85 ± 10	0.62 ± 0.08	10.5 ± 1.0	73 ± 8	0.186 ± 0.103
600 Si	C	3.57 ± 0.14	83 ± 6	0.54 ± 0.03	2.8 ± 0.2	33 ± 4	0.0 ± 0.017
600 Si	Cu	14.3 ± 0.4	90 ± 4	0.41 ± 0.02	14.3 ± 0.5	19.9 ± 1.5	0.0 ± 0.008
600 Si	Pb	55.2 ± 1.5	100 ± 4	0.213 ± 0.021	69.0 ± 1.5	12.7 ± 0.6	0.0 ± 0.018

Table V
Parameters from fits to the indicated angular distributions using Eqn. 5.

Beam (AMeV)	Target	a_1 (b/sr)	a_2 (1/radian)	a_3 (b/sr)	a_4 (1/radian)
230 He	Al	1.76 ± 0.16	4.4 ± 0.8	0.225 ± 0.18	0.72 ± 0.57
230 He	Cu	3.72 ± 0.06	5.96 ± 0.08	0.88 ± 0.01	1.11 ± 0.01
400 N	C	190 ± 150	42 ± 22	3.4 ± 0.3	2.63 ± 0.13
400 N	Cu	34 ± 24	18 ± 8	8.1 ± 0.8	1.92 ± 0.11
400 Kr	Li	4080 ± 1420	39.3 ± 4.1	20.1 ± 2.8	3.49 ± 0.22
400 Kr	C	3940 ± 1570	37.6 ± 4.7	25.7 ± 3.9	3.24 ± 0.23
400 Kr	CH$_2$	6750 ± 2220	37.6 ± 3.9	29.8 ± 5.6	3.25 ± 0.28
400 Kr	Al	4190 ± 2350	35.4 ± 6.6	53.6 ± 8.7	3.21 ± 0.24
400 Kr	Cu	8630 ± 5530	42 ± 13	79 ± 8	2.77 ± 0.14
400 Kr	Pb	(9.6 ± 5.1) x 10^6	114 ± 15	132 ± 13	2.16 ± 0.10
400 Xe	Li	4230 ± 1440	39 ± 4	20.5 ± 3	3.42 ± 0.23
400 Xe	C	3680 ± 900	31.4 ± 3.0	47 ± 9	3.94 ± 0.34
400 Xe	CH$_2$	7260 ± 1900	33 ± 3	43 ± 13	3.38 ± 0.52
400 Xe	Al	2840 ± 780	26.7 ± 3.2	53.4 ± 9.8	3.03 ± 0.26
400 Xe	Cu	3560 ± 1000	26.8 ± 3.3	90 ± 11	2.74 ± 0.16
400 Xe	Pb	7160 ± 6300	32.4 ± 10.2	160 ± 19	2.07 ± 0.13
600 Si	C	156 ± 31	23.1 ± 2.3	5.9 ± 0.7	2.63 ± 0.14
600 Si	Cu	354 ± 117	26.2 ± 3.8	17.8 ± 1.2	2.08 ± 0.07
600 Si	Pb	520 ± 210	24.5 ± 4.5	30.8 ± 1.7	1.28 ± 0.05

Table VI

Total cross sections for the indicated systems. Columns 3 – 5 show the integrated cross sections from 0 to 90 degrees. Column six shows the deduced total cross sections from 0 to 180 degrees.

Beam (AMeV)	Target	> 5 MeV$^{(w/\,c)}$ (barns)	> 10 MeV$^{(w/\,c)}$ (barns)	> 10 MeV$^{(w/o\,c)}$ (barns)	> 10 MeV$^{(0\text{-}180)}$ (barns)
230 He	Al	1.39 ± 0.10	1.28 ± 0.09	1.06 ± 0.07	1.65
230 He	Cu	3.14 ± 0.20	2.68 ± 0.17	2.29 ± 0.14	3.20
400 N	C	3.00 ± 0.20	2.92 ± 0.20	2.70 ± 0.18	2.96
400 N	Cu	11.5 ± 0.8	10.6 ± 0.7	9.7 ± 0.7	11.2
400 Kr	Li	no data	18.8 ± 1.5	17.8 ± 1.4	18.85
400 Kr	C	no data	23.2 ± 1.8	22.4 ± 1.7	23.29
400 Kr	CH$_2$	no data	31.8 ± 2.6	30.7 ± 2.5	31.90
400 Kr	Al	42.4 ± 3.2	41.9 ± 3.1	40.4 ± 3.0	42.10
400 Kr	Cu	71.2 ± 4.9	70.0 ± 4.8	66.3 ± 4.5	70.76
400 Kr	Pb	179 ± 13	168 ± 12	160 ± 12	173.34
400 Xe	Li	no data	28.0 ± 2.3	26.5 ± 2.2	28.02
400 Xe	C	no data	33.6 ± 2.7	32.6 ± 2.6	33.64
400 Xe	CH$_2$	no data	47.4* ± 4.2	46.0* ± 4.0	47.51
400 Xe	Al	no data	52.9 ± 4.2	51.2 ± 4.1	53.19
400 Xe	Cu	no data	90.8 ± 6.5	87.5 ± 6.3	91.73
400 Xe	Pb	no data	210 ± 15	201 ± 15	217.89
600 Si	C	no data	6.20 ± 0.40	5.76 ± 0.37	6.28
600 Si	Cu	24.2 ± 1.5	22.5 ± 1.4	20.4 ± 1.3	23.36
600 Si	Pb	75.7 ± 5.1	66.7 ± 4.4	59.9 ± 4.0	78.21

(w/ c) – includes correction for attenuation of neutron flux
(w/o c) – not corrected for attenuation of neutron flux
* - integrated from 0 to 70 degrees

Table VII

Fit parameters to the total cross sections (0° to 180°) using Eqn. 6.

	C	f_p	f_t	χ^2 (d.o.f.)
He, C, N projectiles	0.014 ± 0.004	1.0 ± 0.5	0.18 ± 0.05	0.61
Ne, Si, Ar projectiles	0.016 ± 0.008	1.0 ± 0.5	0.44 ± 0.21	0.65
Kr, Xe projectiles	0.014 ± 0.006	0.65 ± 0.28	0.78 ± 0.31	0.64
All systems	0.013 ± 0.004	0.90 ± 0.22	0.29 ± 0.08	1.89